Topology optimization of structural systems based on a nonlinear beam finite element model

Navid Changizi[1] · Gordon P. Warn[1] ⓘ

Abstract

A method for the topology optimization of structures composed of nonlinear beam elements based on a hysteretic finite element modeling approach is presented. In the context of the optimal design of structures composed of truss or beam elements, studies reported in the literature have mostly considered linear elastic material behavior. However, certain applications require consideration of the nonlinear response of the structural system to the given external forces. Particular to the methodology suggested in this paper is a hysteretic beam finite element model in which the inelastic deformations are governed by principles of mechanics in conjunction with first-order nonlinear ordinary differential equations. The nonlinear ordinary differential equations determine the onset of inelastic deformations and the approximation of the signum function in the differential equation with the hyperbolic tangent function permits the derivation of analytical sensitivities. The objective of the optimization problem is to minimize the volume of the system such that a system-level displacement satisfies a specified constraint value. This design problem is analogous to that of seismic design where inelastic deformations are permitted, yet sufficient stiffness is required to limit the overall displacement of the system to a specified threshold. The utility of the method is demonstrated through numerical examples for the design of two structural frames and a comparison with the solution from the topology optimization assuming linear elastic material behavior. The comparisons show that the nonlinear design is either comprised of a lower volume for a given level of performance, or offers better performance for a given volume in comparison with optimized linear design.

1 Introduction

Certain design applications require consideration of the nonlinear structural response, e.g., material inelasticity or buckling, to ensure the design meets specific requirements. For example, when designing structural systems for seismic excitation, the systems are intentionally permitted to undergo inelastic deformations while not exceeding specified drift limits (ASCE 2017). Although a substantial body of literature exists on the design of structural systems by topology optimization (Bendsoe and Sigmund 2004) spanning from early work by Miche (1904), to more

recent advancements in methodological developments and applications (Sigmund 1994; Le et al. 2010; Asadpoure et al. 2011; Deaton and Grandhi 2014), these studies often invoke the assumption of linear elastic material response. More recently, studies have relaxed the elastic material assumption (e.g., Nakshatrala and Tortorelli 2015; Alberdi and Khandelwal 2017) explicitly considering inelastic material response. However, existing literature considering material inelasticity has focused almost entirely on continuum. In this paper, a method for the topology optimization of nonlinear structural systems composed of beam elements considering material inelasticity is presented. Material inelasticity is modeled using a hysteretic beam finite element (FE) formulation (Triantafyllou and Koumousis 2011, 2012). The objective of the topology optimization formulation is to minimize the total volume, that can be considered a proxy for the cost of the structural system, while constraining the system-level deformation.

A benefit of the hysteretic beam FE formulation, in the context of topology optimization, is that it permits

---

the derivation of continuous and differentiable sensitivities facilitating the use of gradient-based optimization algorithms as described in detail in this paper. Similar to the established FE approach (Bathe 2006), the hysteretic FE method uses displacement interpolation functions to relate nodal degrees-of-freedom (DOF) to internal strain fields within each element. Unique to the hysteretic FE approach, however, are the addition of hysteretic DOF and associated hysteretic interpolation functions that distribute the inelastic response along the length of the element. The hysteretic DOF are governed by first-order nonlinear ordinary differential equations (ODEs), commonly referred to as evolution equations, and determine the onset of material inelasticity (Sivaselvan and Reinhorn 2000; Triantafyllou and Koumousis 2011). An additional benefit of the hysteretic FE formulation is that it offers computational efficiency, especially for transient excitation, due to the constant elastic stiffness and hysteretic matrices, which are evaluated only once at the outset of the analysis, and do not require updating throughout. Furthermore, in the context of topology optimization, this means their associated sensitivities with respect to the design variable, also only need to be evaluated for each nonlinear analysis.

Literature pertaining to nonlinearity in topology optimization has generally focused on continuum structures employing elasto-plastic or plasticity formulations. Several of these past studies have developed methods and/or analytical sensitivities for history-dependent problems for finite strain under quasi-static conditions (Tortorelli 1992; Maute et al. 1998; Yuge et al. 1999; Nakshatrala et al. 2013; Zhang et al. 2017a), transient excitation and dynamic conditions (Nakshatrala and Tortorelli 2015; Alberdi et al. 2018), and for considering both material and kinematic nonlinearities (Kleiber 1993; Tsay and Arora 1990; Schwarz et al. 2001; Wallin et al. 2016). Furthermore, recent studies have suggested combining the areas of nonlinear topology optimization of continuum structures and damage mechanics for the design of damage resistant structures (Achtziger and Bendsøe 1995; James and Waisman 2014, 2015; Alberdi and Khandelwal 2017; Li et al. 2017, 2018; Li and Khandelwal 2017). For this class of problems a damage model and local damage constraints are typically incorporated into the design problem to achieve damage resistant designs.

A few studies have considered nonlinearity for the topology optimization of frame structures. An early work by Yuge and Kikuchi (1995) studied the optimal design of frame structures considering plastic deformations. In the Yuge and Kikuchi (1995) study, two-dimensional structures were represented by a periodic microstructure where the stress field was obtained from an elasto-plastic FE analysis based on the homogenization method and plastic deformations followed plastic flow theory.

In another work, Pedersen (2003) studied plasticity in topology optimization in the context of crashworthiness, where a ground structure composed of two-dimensional beam elements with rectangular solid cross sections was considered and optimized to maximize energy absorption. In the Pedersen (2003) study, plastic deformations were assumed to be concentrated at the ends of the beam elements and the plastic deformations modeled using conventional plastic flow theory. Later, Pedersen (2004) extended the method to account for distributed plasticity in the beam elements. Others have studied nonlinear elastic and hyperelastic materials in continuum (Klarbring and Strömberg 2013; Luo et al. 2015) and discrete uniaxial truss element systems (Ramos and Paulino 2015; Zhang et al. 2017b). Multi-material design considering material nonlinearity has also been suggested for periodic structures (Swan and Kosaka 1997) and for truss structures (Zhang et al. 2018). However, the assumption of nonlinear elastic material behavior is not suitable when inelastic deformations are expected as is the case when designing structures to resist seismic ground motion.

Here we present, a method for the topology optimization of nonlinear structural systems composed of beam elements considering inelastic material behavior. As mentioned previously, the method combines topology optimization with a hysteretic FE approach to model the inelastic material behavior and as such original mathematical formulations and analytical sensitivities necessary to employ this modeling framework for the design of structural systems are presented. For this study, the ground structure approach, widely used for the topology optimization of structures is employed (Bendsoe and Sigmund 2004; Rozvany and Lewinski 2014). Nonlinear quasi-static analysis is carried out using the hysteretic beam FE model and an iterative solution scheme. As has been suggested by Kim et al. (2003) and Gömöry et al. (2009) for different applications, the hyperbolic tangent function is suggested as a suitable approximation of the signum function in the hysteretic evolution equations, to ensure these functions are continuous and differentiable everywhere. As such, analytical sensitivities with respect to the design variable were derived by direct differentiation. Numerical design examples are presented for the quasi-static case to demonstrate the utility of the method, where the objective of the design is to minimize the volume in a given domain for a given external force(s) subject to a specified system-level displacement constraint. For comparison, linear minimum compliance topology optimization problem is solved to obtain an optimal linear design solution using the optimal volume of the nonlinear design. Nonlinear analysis is performed with the linear minimum compliance design for the same level of external force and the results are compared

with that of the nonlinear volume minimization design to study and illustrate the impact of explicitly considering material inelasticity in the optimization problem.

The remainder of the paper is organized as follows. Section 2 presents the overall methodology, beginning with a discussion on the nonlinear FE modeling approach in the context of beam elements. This discussion is followed by the design formulation for topology optimization of structural systems considering material inelasticity, solution schemes for the nonlinear analysis and sensitivities with respect to the design variables. Section 3 presents the numerical examples and associated results whereby the methodology is applied for the design of structural systems for static excitation including discussions of the results and observations. Lastly, in Section 4, a summary and description of the main contributions and findings are provided.

2 Methodology

The proposed method consists of three main components, specifically nonlinear structural analysis employing the hysteretic beam FE model, the optimization problem formulation, and the corresponding sensitivities to facilitate gradient-based optimization. Evaluation of the performance of a given system relies on the nonlinear static analysis employing the hysteretic beam FE model and provides the basis for the derivation of the sensitivities, hence important details of the modeling approach are described in the subsequent section for the benefit of the remainder of the paper. Herein, boldface upper and lower case font denote matrix and vector quantities, respectively.

2.1 Nonlinear beam FE model

Given the focus of this study being on the optimization of frame structures, an appropriate nonlinear beam FE model that is able to simulate inelastic behavior of beam elements is required. Here the hysteretic beam FE model suggested by Triantafyllou and Koumousis (2012) is adopted. The hysteretic FE approach is the result of efforts by various researchers to extend hysteretic models governed by first-order ODEs (Bouc 1967; Baber and Wen 1981; Baber and Noori 1985; Foliente 1995) beyond the uniaxial case toward established mechanics frameworks including an integrated hysteretic beam FE formulation (Triantafyllou and Koumousis 2011, 2012), multi-axial plasticity (Casciati 1989; Sivaselvan and Reinhorn 2000) and more recently a consistent nonlinear Timoshenko beam FE formulations (Amir et al. 2019). For a detailed derivation of the model formulations, the interested reader is referred to the aforementioned studies.

Like the conventional displacement-based FE approach (Bathe 2006), the hysteretic FE method employs displacement interpolation functions, however, there are additional hysteretic DOF and associated interpolation functions that differentiate the hysteretic FE modeling approach from conventional methods. This section summarizes the general concept and notable details of the hysteretic beam FE model. Additional details, definitions, and relationships necessary to complete the formulation can be found in Appendices 1 and 2. The model employed here is based upon a two-node Euler-Bernoulli beam element with length L as illustrated in Fig. 1. The beam element has three independent displacement DOF for each node, namely longitudinal u, transverse w and rotation θ; however, unique to this FE modeling approach are hysteretic DOF, $\mathbf{z}$, in addition to the traditional displacement DOF. Two hysteretic DOF are considered for each node, specifically z_u and z_ϕ corresponding to longitudinal and rotational deformations, respectively. Thus, the element displacement and hysteretic DOF vectors can be defined as:

$$\mathbf{d}^{el} = \begin{bmatrix} u_1 & w_1 & \theta_1 & u_2 & w_2 & \theta_2 \end{bmatrix}^T$$
$$\mathbf{z}^{el} = \begin{bmatrix} z_{u1} & z_{\phi1} & z_{u2} & z_{\phi2} \end{bmatrix}^T, \tag{1}$$

where the superscripts e and l denote element-level and DOF with respect to the element local coordinates, respectively. Subscripts 1 and 2 correspond to the start and end nodes, respectively. Herein, superscripts e and l are only shown when necessary to differentiate element from system-level and local from global coordinates. Assuming a prismatic beam element, the internal stress resultants at a
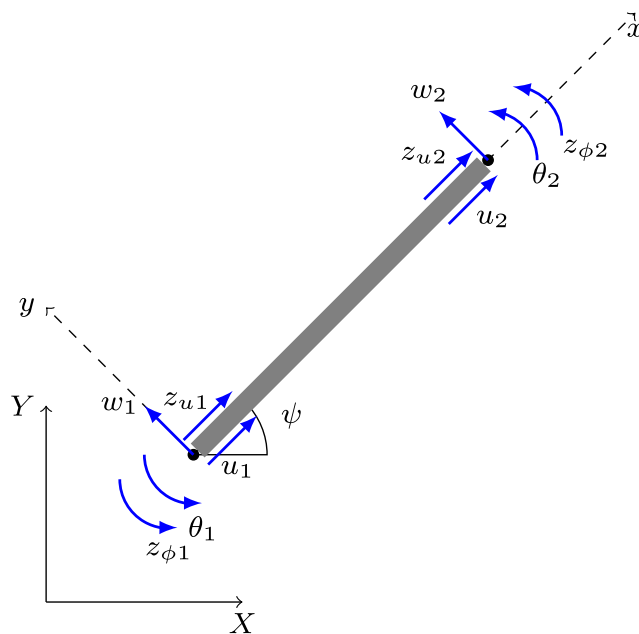

Fig. 1 Illustration of a two-node beam element and corresponding displacement and hysteretic DOF

given point x along the length of the element are given by the following set of hysteretic laws:

$$P(x) = \alpha_u Ea\epsilon_u(x) + (1 - \alpha_u)Eaz_u(x)$$
$$M(x) = \alpha_\phi EI\epsilon_\phi(x) + (1 - \alpha_\phi)EIz_\phi(x), \qquad (2)$$

where $P(x)$ and $M(x)$ correspond to axial force and bending moment, respectively. The stress resultants in (2) can be viewed as the sum of two parallel components, the first component contributing to the post-elastic kinematic hardening and the second is the nonlinear component simulating the hysteretic behavior according to the hysteretic DOF ($z_u(x)$ and $z_\phi(x)$). Variables $\epsilon_u(x)$ and $\epsilon_\phi(x)$ are the axial strain and curvature, respectively; E, I, and a are the elastic modulus, moment of inertia, and cross-sectional area of the beam element, respectively; and α_u and α_ϕ are the ratio of post-elastic to elastic modulus for axial and bending deformations, respectively.

The hysteretic DOF evolved according to a set of nonlinear ODEs, commonly referred to as evolution equations, that for the axial deformation and curvature are expressed as:

$$\dot{z}_u(x) = (1 - H_{1u}(x)H_{2u}(x))\,\dot{\epsilon}_u(x)$$
$$\dot{z}_\phi(x) = \left(1 - H_{1\phi}(x)H_{2\phi}(x)\right)\dot{\epsilon}_\phi(x), \qquad (3)$$

where $H_{1u}(x)$ and $H_{1\phi}(x)$ are functions given by:

$$H_{1u}(x) = \left|\frac{P^h(x)}{P_c^h}\right|^n, \qquad H_{1\phi}(x) = \left|\frac{M^h(x)}{M_c^h}\right|^n. \qquad (4)$$

In (4), $P^h(x)$ is the current hysteretic axial force, P_c^h is the hysteretic axial force capacity, $M^h(x)$ is the current hysteretic bending moment, M_c^h is the hysteretic bending moment capacity and n is a hysteretic parameter that controls the transition between elastic and inelastic branches. Furthermore, $H_{2u}(x)$ and $H_{2\phi}(x)$ in Eq. 3 are heaviside functions expressed as follows:

$$H_{2u}(x) = \gamma\,\text{sgn}\left(P^h(x)\dot{\epsilon}_u(x)\right) + \beta$$
$$H_{2\phi}(x) = \gamma\,\text{sgn}\left(M^h(x)\dot{\epsilon}_\phi(x)\right) + \beta, \qquad (5)$$

where $\text{sgn}(\cdot)$ is the signum function and β and γ are parameters that control the relationship between the loading and unloading stiffness. Specifying the hysteretic parameters to satisfy the following constraints of $\beta + \gamma = 1$ and $-\gamma \leq \beta \leq \gamma$ have been proven to result in a thermodynamically admissible model (Erlicher and Point 2004). Hence, in this study, both β and γ are set equal to 0.5 that results in the loading and unloading stiffnesses being equal in addition to satisfying the parameter constraints. To consolidate the notation into more compact expressions, the hysteretic laws shown in (2) are expressed in matrix format as:

$$\mathbf{m}^{el}(x) = \mathbf{D}\boldsymbol{\epsilon}(x) + \mathbf{D}^h\mathbf{z}^{el}(x), \qquad (6)$$

where the components of $\mathbf{m}^{el}(x)$ are arranged as $\mathbf{m}^{el}(x) = [P(x)\ M(x)]^T$, and matrices $\mathbf{D}$ and $\mathbf{D}^h$ are the elastic and hysteretic rigidity matrices whose elements are functions of the material and the cross sectional properties. Similarly, the evolution equations shown in (3) are compactly expressed in matrix format as follows:

$$\dot{\mathbf{z}}^{el}(x) = (\mathbf{I}_{2\times2} - \mathbf{S}(x))\,\dot{\boldsymbol{\epsilon}}(x), \qquad (7)$$

where $\mathbf{I}$ is identity matrix and the matrix $\mathbf{S}(x)$ is defined in (8).

$$\mathbf{S}(x) = \begin{bmatrix} H_{1u}(x)H_{2u}(x) & 0 \\ 0 & H_{1\phi}(x)H_{2\phi}(x) \end{bmatrix}. \qquad (8)$$

Following the displacement-based FE approach, the conventional cubic displacement interpolation functions are used to relate nodal displacements to the local deformation fields at a given location along the length of the element but are omitted here for brevity (see Bathe 2006). Assuming axial force is constant along the length of the element, that the bending moment varies linearly, and applying the appropriate hysteretic boundary conditions, the interpolation functions for the hysteretic DOF, $\mathbf{z}^{el}$ are expressed as:

$$z_u(x) = \begin{bmatrix} 0.5 & 0.5 \end{bmatrix}\begin{bmatrix} z_{u1} \\ z_{u2} \end{bmatrix}$$
$$z_\phi(x) = \begin{bmatrix} 1 - \frac{x}{L} & \frac{x}{L} \end{bmatrix}\begin{bmatrix} z_{\phi1} \\ z_{\phi2} \end{bmatrix}. \qquad (9)$$

The hysteretic interpolation functions shown in (9) serve to distribute the inelasticity along the length of the element. Substituting the hysteretic laws in (2), the interpolation functions and their derivatives into the variational principle of virtual work expressed for a given location x along the length of the beam element, performing the required integration by parts and enforcing the integration limits of 0 and L, the following element elastic stiffness matrix and hysteretic matrix are obtained:

$$\mathbf{K}^{el} = E\begin{bmatrix} \frac{\alpha_u a}{L} & 0 & 0 & \frac{-\alpha_u a}{L} & 0 & 0 \\ 0 & \frac{12\alpha_\phi I}{L^3} & \frac{6\alpha_\phi I}{L^2} & 0 & -\frac{12\alpha_\phi I}{L^3} & \frac{6\alpha_\phi I}{L^2} \\ 0 & \frac{6\alpha_\phi I}{L^2} & \frac{4\alpha_\phi I}{L} & 0 & -\frac{6\alpha_\phi I}{L^2} & \frac{2\alpha_\phi I}{L} \\ \frac{-\alpha_u a}{L} & 0 & 0 & \frac{\alpha_u a}{L} & 0 & 0 \\ 0 & -\frac{12\alpha_\phi I}{L^3} & -\frac{6\alpha_\phi I}{L^2} & 0 & \frac{12\alpha_\phi I}{L^3} & -\frac{6\alpha_\phi I}{L^2} \\ 0 & \frac{6\alpha_\phi I}{L^2} & \frac{2\alpha_\phi I}{L} & 0 & -\frac{6\alpha_\phi I}{L^2} & \frac{4\alpha_\phi I}{L} \end{bmatrix}$$

$$\mathbf{H}^{el} = E\begin{bmatrix} \frac{(\alpha_u-1)a}{2} & 0 & \frac{(\alpha_u-1)a}{2} & 0 \\ 0 & \frac{(\alpha_\phi-1)I}{L} & 0 & -\frac{(\alpha_\phi-1)I}{L} \\ 0 & (\alpha_\phi-1)I & 0 & 0 \\ -\frac{(\alpha_u-1)a}{2} & 0 & -\frac{(\alpha_u-1)a}{2} & 0 \\ 0 & -\frac{(\alpha_\phi-1)I}{L} & 0 & \frac{(\alpha_\phi-1)I}{L} \\ 0 & 0 & 0 & -(\alpha_\phi-1)I \end{bmatrix}. \qquad (10)$$

Thus, the element force deformation relationship in local coordinates can be compactly expressed as:

$$\mathbf{K}^{el}\mathbf{d}^{el} + \mathbf{H}^{el}\mathbf{z}^{el} = \mathbf{f}^{el}. \tag{11}$$

To proceed to the solution of the system-level equations in global coordinates, both $\mathbf{K}^{el}$ and $\mathbf{H}^{el}$ must be transformed to the global coordinates system which can be accomplished according to the following expressions:

$$\mathbf{K}^{e} = \boldsymbol{\Lambda}^{T}\mathbf{K}^{el}\boldsymbol{\Lambda}, \quad \mathbf{H}^{e} = \boldsymbol{\Lambda}^{T}\mathbf{H}^{el}, \tag{12}$$

where $\boldsymbol{\Lambda}$ is the conventional 6×6 transformation matrix for beam element (Bathe 2006). After performing the appropriate transformations and mapping, the global force-displacement equations are expressed as follows:

$$\mathbf{Kd} + \mathbf{Hz} = \mathbf{f}, \tag{13}$$

where $\mathbf{K}$ and $\mathbf{d}$ are the stiffness matrix and displacement vector respectively, $\mathbf{H}$ and $\mathbf{z}$ are the hysteretic matrix and the hysteretic vector, respectively, and $\mathbf{f}$ is a vector of external nodal forces all in global coordinates. After assembling the global matrices, boundary conditions are imposed in the usual manner to obtain the system matrices via the typical direct stiffness assembly method. A benefit of this hysteretic FE modeling approach, in comparison with the more typical plasticity approach, is that the matrices $\mathbf{K}$ and $\mathbf{H}$ only need to be evaluated once, at the outset of the nonlinear analysis and otherwise remain constant.

The gradient-based optimization requires sensitivities of the objective function and constraints with respect to the design variables. For computational efficiency, it is preferable to use analytical sensitivities to numerical approximations and this point is one of the motivations for employing the hysteretic beam FE model. However, the exact form of the nonlinear ODEs shown in (7) includes the signum function. Hence, a mathematical approximation is introduced in order to obtain analytical sensitivities that are continuous and differentiable everywhere. Here, the hyperbolic tangent function is introduced as an approximation for the signum function according to:

$$
\begin{aligned}
H_{2u} &= \gamma \tanh(\zeta P^{h}\dot{\epsilon}_{u}) + \beta \\
H_{2\phi} &= \gamma \tanh(\zeta M^{h}\dot{\epsilon}_{\phi}) + \beta,
\end{aligned} \tag{14}
$$

where ζ is a coefficient that controls the shape of the hyperbolic tangent function in the proximity of zero. Assigning a large numerical value to ζ, closely approximates the signum function shape yet remains differentiable. In this study, a value of 50 is specified for ζ.

2.2 Optimization problem

The design problem considered here seeks to minimize the volume of the structural system subject to a system-level displacement constraint. Hence, having the nonlinear beam FE model, the volume minimization topology optimization problem considering material inelasticity subject to a system-level displacement constraint can be expressed as:

$$
\begin{aligned}
&\text{Find:} && a_1, ..., a_N \\
&\underset{\mathbf{a}}{\text{Minimize:}} && v = \sum_{s=1}^{N} a_s L_s \\
&\text{Subject to:} && \mathbf{Kd} + \mathbf{Hz} = \mathbf{f} \\
& && d_v \leq d^* \\
& && 0 < \rho_{\min} < a \leq \rho_{\max},
\end{aligned} \tag{15}
$$

where v is the volume in the domain, $\mathbf{a}$ is a vector of design variables representing the individual element cross-sectional areas and N is the number of elements, for a given iteration in the optimization process. Here, equilibrium of the structural system and the system-level displacement are imposed as constraints which relate the response of the system to the design variables. Nonlinear static analysis is performed to establish equilibrium of the system and to evaluate the response, which is the displacement at a specific degree of freedom, d_v, here representing the system-level deformation which is constrained to a threshold value d^*. Each element's cross-sectional area, a_s, is also constrained in (15) between $\rho_{\min}$ and $\rho_{\max}$. The lower limit $\rho_{\min}$ avoids singularity during the optimization process and the upper limit is based on the maximum cross sectional area available for I-shaped sections in American Institute of Steel Construction (2015). An approach for relating the cross-sectional area to other geometric properties for I-shaped cross sections suggested by Changizi and Jalalpour (2017b) is adopted in this study and the regression curves for the median range are used for the optimization process.

2.2.1 Nonlinear analysis

Nonlinear static analysis is employed to determine the unknown DOF, $\mathbf{d}$ and $\mathbf{z}$. Each nonlinear static analysis is performed in a step-wise fashion until the specified external force value is attained. A challenge when material inelasticity is considered, is the iterative, and hence computationally expensive analysis, which is often required. For this study, a Newton solution scheme is devised for the hysteretic FE model and the nonlinear static analysis whereby for each force step, the unknowns (that is $\mathbf{d}$ and $\mathbf{z}$) are iteratively updated until the norm of the residual vector falls below the specified tolerance. For the solution scheme, the equilibrium equations and hysteretic evolution equations are combined into a single system of nonlinear equations whereby the unknown displacement and hysteretic DOF are simultaneously updated in an iterative manner. We define

a vector, $\mathbf{x}_{i+1}^{j+1}$, which is an augmented set of unknowns containing $\mathbf{d}$ and $\mathbf{z}$ as:

$$\mathbf{x}_{i+1}^{j+1} = \begin{bmatrix} \mathbf{d}_{i+1}^{j+1} \\ \mathbf{z}_{i+1}^{j+1} \end{bmatrix}, \tag{16}$$

where i represents the ith force-step and j represents the jth iteration of the ith force step. For a given force step, the vector of unknowns, $\mathbf{x}_{i+1}^{j+1}$, is updated according to the following expression:

$$\mathbf{x}_{i+1}^{j+1} = \mathbf{x}_{i+1}^{j} - \mathbf{J}_v^{-1}\mathbf{g}_v, \tag{17}$$

where $\mathbf{J}_v$ and $\mathbf{g}_v$ are the Jacobian matrix and residual vector, respectively, each subsequently defined. For a quasi-static analysis, the rate of change of the hysteretic DOF and strains are approximated using the following backward difference expressions to convert the nonlinear ODEs into a set of algebraic expressions conducive to the Newton update:

$$\dot{\mathbf{z}}_{i+1}^{el} = \frac{\Delta \mathbf{z}^{el}}{\Delta t} = \frac{\mathbf{z}_{i+1}^{el} - \mathbf{z}_i^{el}}{\Delta t}$$
$$\dot{\boldsymbol{\epsilon}}_{i+1} = \frac{\Delta \boldsymbol{\epsilon}}{\Delta t} = \frac{\boldsymbol{\epsilon}_{i+1} - \boldsymbol{\epsilon}_i}{\Delta t}, \tag{18}$$

where Δt represents pseudo time that is, nevertheless, eliminated from the equations through algebra. Substituting (18) into (7), the following expression is obtained that relates $\mathbf{z}_{i+1}^{el}$ to $\boldsymbol{\epsilon}_{i+1}$ for the two-node beam element:

$$\mathbf{z}_{i+1}^{el} = \mathbf{z}_i^{el} + (\mathbf{I}_{2\times2} - \mathbf{S})\,\Delta\boldsymbol{\epsilon}, \tag{19}$$

and the equilibrium equation at step $i+1$ can be written as:

$$\mathbf{K}\mathbf{d}_{i+1}^{j} + \mathbf{H}\mathbf{z}_{i+1}^{j} = \mathbf{f}_{i+1}. \tag{20}$$

Thus, the combined system of equations, which is the equilibrium (20) and the hysteretic evolution (19), is expressed compactly for the Newton update as:

$$\mathbf{g}_v = \mathbf{q}_v + \mathbf{T}_v\mathbf{x}_{i+1}^{j} - \mathbf{c}_v. \tag{21}$$

The quantities $\mathbf{q}_v$, $\mathbf{T}_v$ and $\mathbf{c}_v$ are expressed as follows:

$$\mathbf{q}_v = \begin{bmatrix} \mathbf{0}_{3r\times1} \\ \mathbf{g}_z \end{bmatrix}, \quad \mathbf{T}_v = \begin{bmatrix} \mathbf{K} & \mathbf{H} \\ -\mathbf{R} & \mathbf{I}_{3r\times4N} \end{bmatrix}$$
$$\mathbf{c}_v = \begin{bmatrix} \mathbf{f}_{i+1} \\ \mathbf{g}_{zc} \end{bmatrix}, \tag{22}$$

where r is the number of nodes in the domain. The quantities $\mathbf{g}_z$, $\mathbf{R}$ and $\mathbf{g}_{zc}$ are assembly matrices of the following element-level relations:

$$\mathbf{g}_z^e = \mathbf{S}\Delta\boldsymbol{\epsilon}, \quad \mathbf{R}^e = \mathbf{B}\Lambda, \quad \mathbf{g}_{zc}^e = \mathbf{z}_i - \boldsymbol{\epsilon}_i, \tag{23}$$

where $\mathbf{B}$ is the strain-displacement matrix for the beam element. Lastly, the Jacobian matrix, $\mathbf{J}_v$, is evaluated according to (24):

$$\frac{\partial\mathbf{g}_v}{\partial\mathbf{x}_{i+1}^{j}} = \mathbf{J}_v = \mathbf{T}_v + \mathbf{J}_{vn}, \tag{24}$$

where $\mathbf{J}_{vn}$ is the part of the Jacobian matrix with complete derivation provided in Appendix 3. With all associated terms sufficiently defined in (16) through (24), the system of nonlinear equations can be solved for each iteration of the optimization process to determine the DOF of the system, $\mathbf{d}$ and $\mathbf{z}$, for a specified external force, $\mathbf{f}$.

2.2.2 Sensitivities

The use of gradient-based optimization necessitates sensitivities with respect to the design variable, a. The sensitivity of the objective function is obtained in a straightforward manner and is omitted here for brevity. The main challenge in deriving the sensitivities arises from the nonlinear constraint on the system-level displacement. Sensitivities for the displacement constraint were derived through direct differentiation and begins with the differentiation of the augmented vector, $\mathbf{x}_{i+1}^{j+1}$, with respect to a and continues with the differentiation of all subsequent terms to obtain the analytical expressions for the sensitivities. The key steps of the derivation are provided here and additional details for the complete derivation are given in Appendix 4. The derivative of system-level displacement constraint is a component of:

$$\frac{\partial\mathbf{x}_{i+1}^{j+1}}{\partial a} = \begin{bmatrix} \frac{\partial\mathbf{d}_{i+1}^{j+1}}{\partial a} \\ \frac{\partial\mathbf{z}_{i+1}^{j+1}}{\partial a} \end{bmatrix}, \tag{25}$$

where this derivative is obtained by differentiation of (17) according to:

$$\frac{\partial\mathbf{x}_{i+1}^{j+1}}{\partial a} = \frac{\partial\mathbf{x}_{i+1}^{j}}{\partial a} + \mathbf{J}_v^{-1}\frac{\partial\mathbf{J}_v}{\partial a}\mathbf{J}_v^{-1}\mathbf{g}_v - \mathbf{J}_v^{-1}\frac{\partial\mathbf{g}_v}{\partial a}, \tag{26}$$

and the derivative of the Jacobian matrix, $\partial\mathbf{J}_v/\partial a$, is:

$$\frac{\partial\mathbf{J}_v}{\partial a} = \frac{\partial\mathbf{T}_v}{\partial a} + \frac{\partial\mathbf{J}_{vn}}{\partial a}. \tag{27}$$

The third term in (26), $\partial\mathbf{g}_v/\partial a$, is obtained by differentiating (21) as follows:

$$\frac{\partial\mathbf{g}_v}{\partial a} = \frac{\partial\mathbf{q}_v}{\partial a} + \frac{\partial\mathbf{T}_v}{\partial a}\mathbf{x}_{i+1}^{j} + \mathbf{T}_v\frac{\partial\mathbf{x}_{i+1}^{j}}{\partial a} - \frac{\partial\mathbf{c}_v}{\partial a}. \tag{28}$$

As indicated by (28), the derivatives of the expressions in (22) for $\mathbf{q}_v$, $\mathbf{T}_v$ and $\mathbf{c}_v$ are required and are expressed as:

$$\frac{\partial\mathbf{q}_v}{\partial a} = \begin{bmatrix} \mathbf{0}_{3r\times1} \\ \frac{\partial\mathbf{g}_z}{\partial a} \end{bmatrix}, \quad \frac{\partial\mathbf{T}_v}{\partial a} = \begin{bmatrix} \frac{\partial\mathbf{K}}{\partial a} & \frac{\partial\mathbf{H}}{\partial a} \\ \mathbf{0}_{4N\times3r} & \mathbf{0}_{4N\times4N} \end{bmatrix}$$
$$\frac{\partial\mathbf{c}_v}{\partial a} = \begin{bmatrix} \mathbf{0}_{3r\times1} \\ \frac{\partial\mathbf{g}_{zc}}{\partial a} \end{bmatrix}, \tag{29}$$

where $\partial \mathbf{g}_z / \partial a$ is an assembly of the following element-level derivatives:

$$\frac{\partial \mathbf{g}_z^e}{\partial a} = \frac{\partial \mathbf{S}}{\partial a} \Delta \boldsymbol{\epsilon} + \mathbf{S} \frac{\partial \Delta \boldsymbol{\epsilon}}{\partial a}$$

$$\frac{\partial \mathbf{S}}{\partial a} = \begin{bmatrix} \frac{\partial H_{1u}}{\partial a} H_{2u} + H_{1u} \frac{\partial H_{2u}}{\partial a} & 0 \\ 0 & \frac{\partial H_{1\phi}}{\partial a} H_{2\phi} + H_{1\phi} \frac{\partial H_{2\phi}}{\partial a} \end{bmatrix},$$

(30)

and similarly, $\partial \mathbf{g}_{zc} / \partial a$ is obtained using the element expression given by:

$$\frac{\partial \mathbf{g}_{zc}^e}{\partial a} = \frac{\partial \mathbf{z}_i^{el}}{\partial a} - \frac{\partial \boldsymbol{\epsilon}_i}{\partial a}, \qquad \frac{\partial \boldsymbol{\epsilon}_i}{\partial a} = \mathbf{B} \boldsymbol{\Lambda} \frac{\partial \mathbf{d}_i^e}{\partial a}.$$

(31)

Equations (26)–(31), and the derivative of the objective omitted, comprise the analytical sensitivities for the volume minimization design formulation.

2.3 Solution of the topology optimization process

With the requisite components having been developed in the previous sections, the problem formulation described in Section 2 for the topology optimization of frame structures considering material inelasticity is applied following the process depicted by the flow diagram shown in Fig. 2. Rather than perform a single phase of optimization and then post-process the results, removing elements with areas less than the minimal constraint value, which could result in a design solution that does not satisfy the constraints, in this study multiple phases of optimization are performed to ensure the final optimized design satisfies the constraints. For each phase of optimization, the gradient-based algorithm employed is the Interior Point algorithm by way of the `fmincon` function in MATLAB (The MathWorks Inc. 2018) with a specified tolerance of 0.0001% on the objective function and the nonlinear constraint. Following the first phase of optimization, element areas are ranked and those with minimal area are removed from the ground structure, but without exceeding a total elements volume of 5% and an updated FE model is generated accordingly for a subsequent phase of optimization. The limit of 5% of the total volume was found to provide an adequate balance between additional computation and egregious degeneration of the solution. No difference in the final solution was observed when testing lower values for this limit, e.g., 2%. To achieve a converged design solution, subsequent phases of the optimization process (see Fig. 2), typically two or three, are performed each starting with the updated design configuration with minimal area elements having been removed. Convergence is achieved when no elements in the optimized design have minimal area, and the topology connectivity remains unchanged throughout a given phase of optimization. For each design application, the nonlinear static analysis is
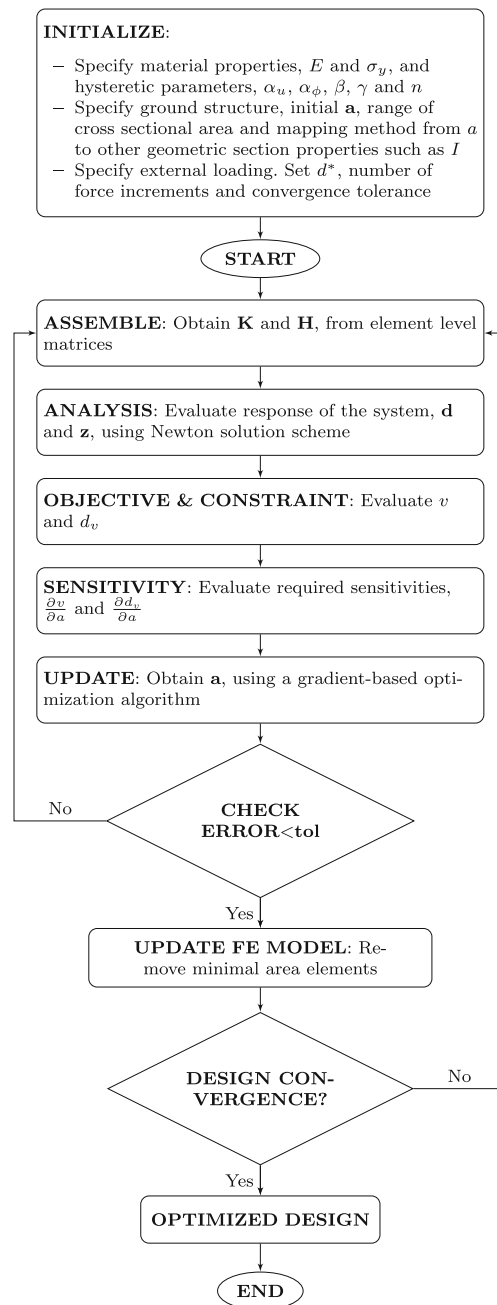

Fig. 2 Flowchart for topology optimization solution scheme

carried out using the iterative Newton solution scheme outlined in the previous section. The specified external force is applied in 20 equal force increments.

Due to the non-convex nature of the volume minimization problem, the global optima cannot be guaranteed. However, in an effort to investigate the non-convexity and gain confidence in the optimized solution, a multi-start strategy where initial values of the design variables are randomly assigned (Boese et al. 1994; Martí et al. 2016) is adopted in this study. For each numerical example, an entire optimization process was conducted for five starting cases, which

is the set of specified initial cross-sectional areas, and the solution from the five optimization processes with the lowest objective function value is considered the best estimate of the global optimal design solution. For each randomized start case, the initial cross-sectional areas are established by sampling the volume for each element from a uniform distribution, from which the cross-sectional area is assigned based upon the elements location in the ground structure. One of the five starting cases assumed the initial cross-sectional area of all elements in the ground structure to be equal, referred to as uniform area.

3 Numerical examples

The utility of the proposed methodology is demonstrated through two representative numerical examples for the design of structural systems composed of beam elements. Details pertaining to the two design examples are provided in this section. As previously stated, the ground structure approach is employed in this study, whereby a dense mesh of connected elements is the initial configuration for the considered design examples. The material is assumed to be steel with Young's modulus of 29,000 ksi and yield stress of 36 ksi. The inelastic to elastic ratios, α_u and α_ϕ, are each set equal to 0.01, and exponent, n, for the hysteretic functions is set equal to 2. The constitutive relationship considered is illustrated by the axial stress versus axial strain, and normalized moment versus curvature relationships shown in Fig. 3. These relationships are obtained using the hysteretic laws (shown in (2)) and the entire response, that is the loading branch, unloading branch and inelastic deformations, are determined by the hysteretic variables that are governed by the hysteretic evolution equations shown in (3). Also shown in Fig. 3, for reference, is a linear elastic response.

3.1 Example 1: a 4 × 2 frame structure

The first example is the design of a 4 × 2 frame structure with a lateral force applied at the top left node of the domain. The ground structure, boundary conditions and direction of applied force are shown in Fig. 4. The dimensions of the domain are $L_x = 19.68$ ft (6 m) and $L_y = 39.4$ ft (12 m).

Prior to each example, the accuracy of the analytical sensitivities developed in Section 2.2.2 was evaluated by comparison with that obtained from a finite difference approximation. The sensitivity values of the displacement constraint for the 4 × 2 frame ground structure are shown in Fig. 5. As is seen from Fig. 5 the derived sensitivities from the two methods agree well with negligible error (less than 0.05%), verifying the accuracy of the analytical sensitivities obtained through the direct differentiation approach.

The minimum volume design problem subject to displacement constraint is solved for the frame structure shown in Fig. 4 for a specified displacement constraint d^* of 11.8 in., equivalent to a drift ratio of 2.5% (i.e., $d^*/L_y = 0.025$) and the specified external force of 500 kips. The optimized design for the $d^* = 0.025L_y$ by starting optimization from the uniform area distribution is shown in Fig. 6, where the thickness of the lines comprising the topologies indicates the relative size of the element area and the area values are normalized with respect to the their maximum among the designs. The numerical value adjacent to each element denote the element number. For this example, a volume of 2.3995×10^4 in.^{3} was required for the nonlinear optimization/design to satisfy the drift constraint.

In addition to the uniform area starting case, as described in Section 2.3, four randomized area starting cases were performed for each numerical example in an attempt to identify the global optima. The optimized topologies obtained for each of the randomized starting
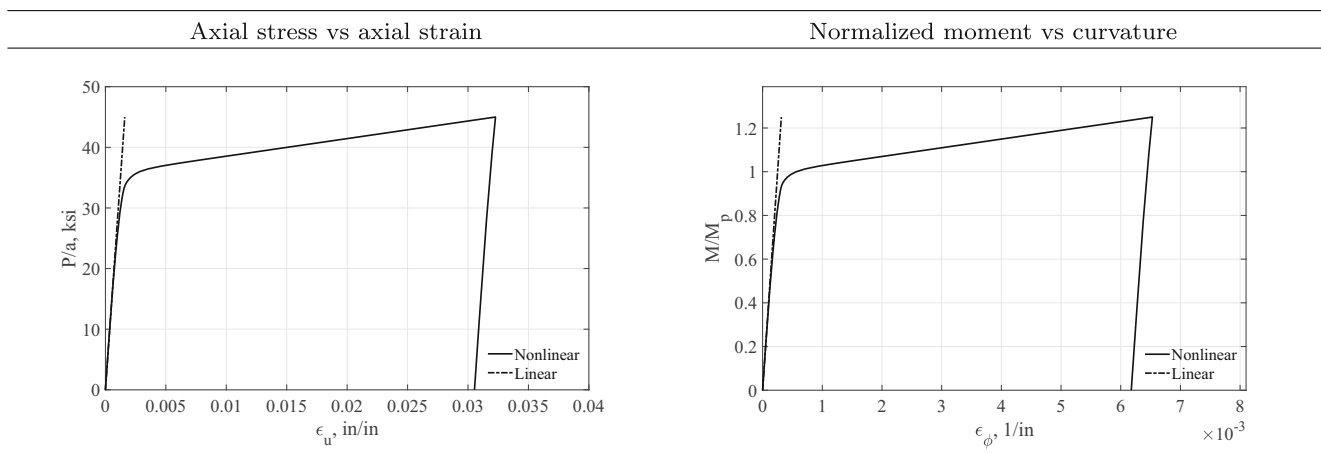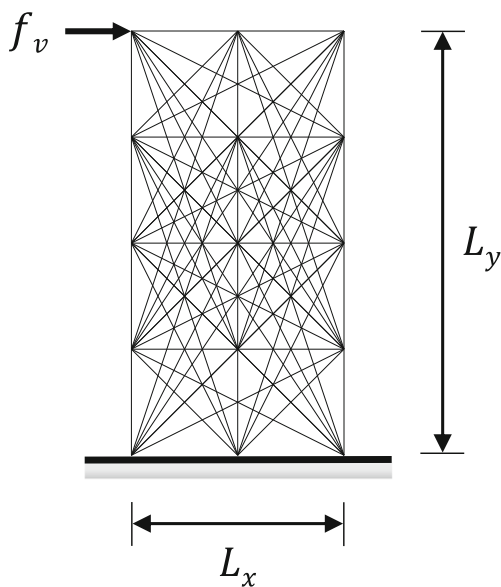
Fig. 3 Axial stress vs axial strain and normalized moment vs curvature relationships
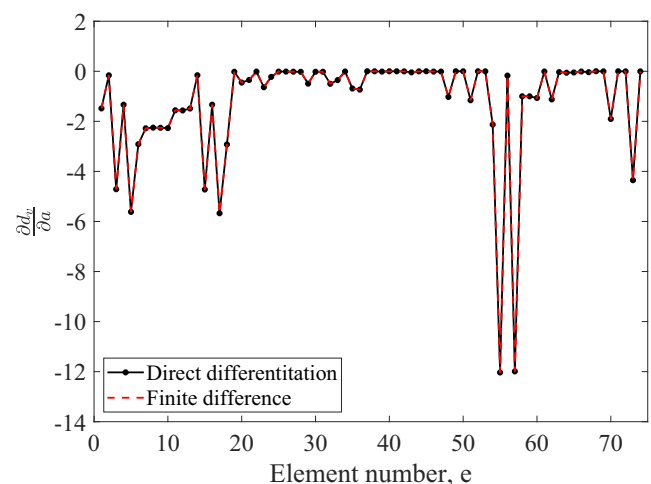
Fig. 4 Ground structure for the 4 × 2 frame structure under a lateral external force

cases, including attributes of the optimized designs, and a plot of the initial randomized areas for the 4 × 2 frame structure are presented in Fig. 7. Numerical values of the initial cross-sectional areas for each starting case are tabulated and reported in Appendix 5. It can be seen from a comparison of the results shown in Fig. 6 with those shown in Fig. 7 that, since all designs satisfy the displacement constraint, $d^* = 11.81$ in., the nonlinear design shown in Fig. 6 is comprised of the lowest volume among the five designs, and hence is considered the best solution.

To investigate the effect of considering material nonlinearity directly in the optimization problem, the best nonlinear design shown in Fig. 6, is compared with the best design solutions from two additional optimization problems considering the same domain and external force but assuming the material to be linear elastic. Specifically, the first linear optimization problem seeks to minimize the compliance for a given volume constraint and the second linear optimization problem seeks to minimize the volume subjected to a drift displacement constraint. These linear design solutions where then evaluated using nonlinear FE analysis described in Section 2.2.1 to assess their respective performance and compare this performance with that of the best nonlinear design. Details pertaining to the two linear optimization formulations can be found in Appendix 6. For both the linear optimization problems, the same multi-start strategy performed for the nonlinear design problem was employed, and the solution with the lowest objective function value was considered the best linear design. Figure 6 shows a comparison of the solution from the nonlinear volume minimization problem, denoted nonlinear design, with the solution of the linear compliance minimization problem, denoted linear

design, and their performance in terms of system force-displacement response when evaluated using nonlinear FE analysis. The linear design is obtained by setting the optimal volume of the nonlinear design as the volume constraint for the linear compliance problem. From Fig. 6 it can be seen that both designs share a common primary load path; however, the nonlinear design includes an additional diagonal element in comparison with the linear design and the proportioning of the individual areas differs between the two designs. For reference, the element with maximum area is from the linear compliance design solution located at element 7 with an area of 31.18 in.[2]. Importantly, from the system force-displacement responses shown in Fig. 6, the nonlinear design satisfies the specified constraint (11.8 in.), whereas the linear design with the same volume of material as the nonlinear design, exceeds the specified constraint when evaluated by nonlinear FE analysis, with a displacement of 15.06, equivalent to a drift ratio of 3.2%, or 27.5% larger than the response of the nonlinear optimized design.

The solution of the second linear optimization problem, that is volume minimization subject to the same displacement constraint (2.5% drift) resulted in a linear design solution with the same general topology as the other linear design shown in Fig. 6 but with a volume of 5.1767×10^3 in.[3]. As anticipated, this volume is considerably smaller than the optimized volume of the nonlinear design. Scaling the linear volume of 5.1767×10^3 in.[3] by a factor of 4.715, without changing the proportioning of the element cross-sectional areas, results in a design based on the linear optimized topology that satisfies the drift constraint when evaluated by nonlinear quasi-static analysis. Interestingly, $4.715 \times 5.1767 \times 10^3 = 2.4408 \times 10^4$ in.[3], exceeds the volume of the nonlinear design of 2.3995×10^4 in.[3]. These

Fig. 5 Comparison of the results of sensitivity analysis derived with the analytical direct differentiation method and finite difference approximation for the 4 × 2 frame ground structure

Nonlinear design, $d^* = 0.025 L_y$	Linear design	Force-displacement response
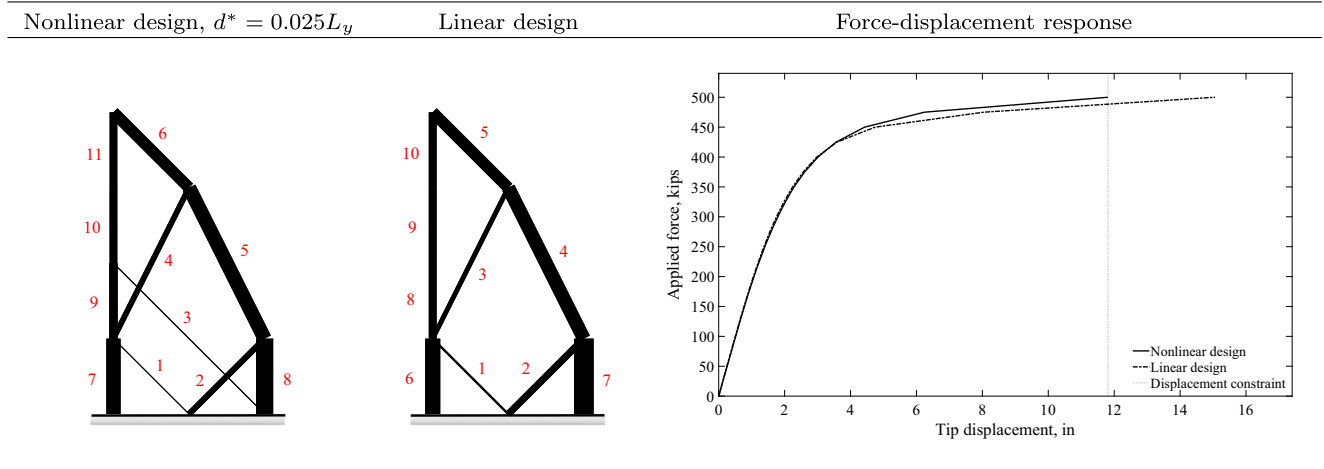
Fig. 6 Nonlinear minimum volume design for 2.5% system drift ratio and comparative linear design with the equivalent volume for the 4×2 frame structure along with the force-d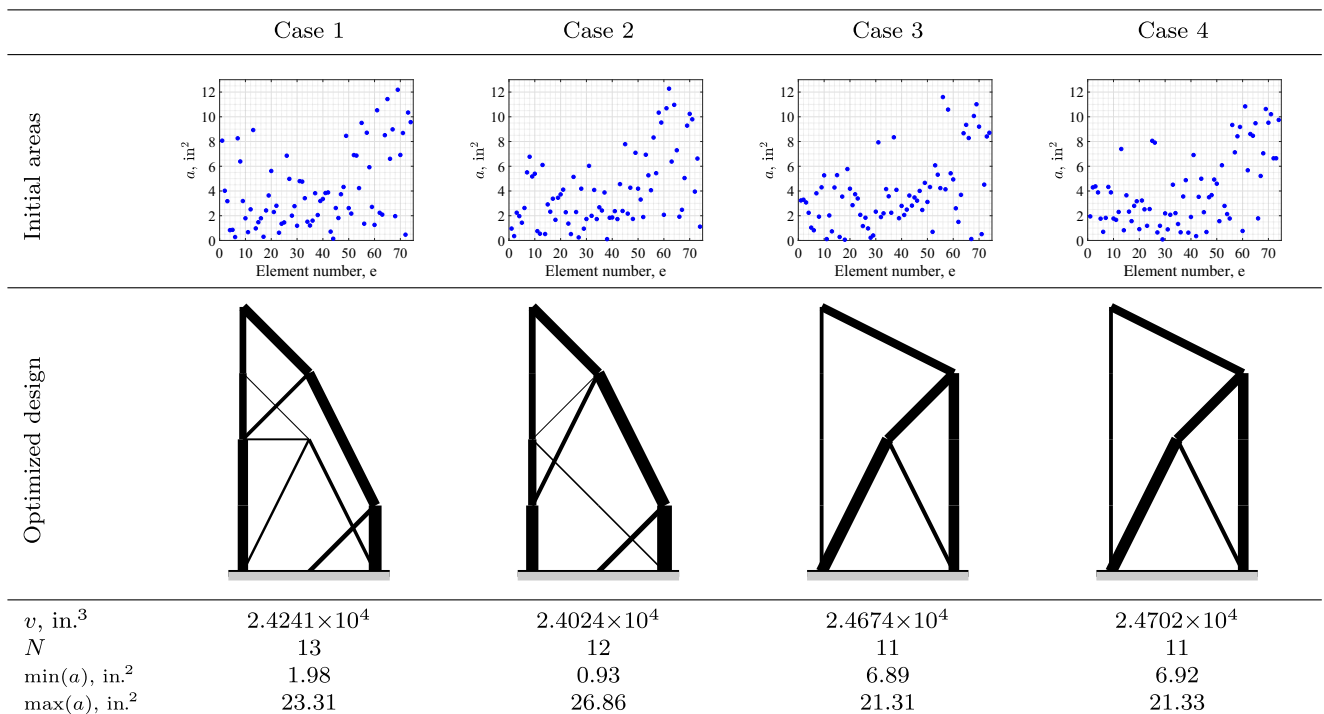isplacement responses for each optimized design. Numerical values adjacent to structural elements denote the element number

comparisons illustrate the nonlinear design offers either better performance for the same volume or lower volume for a given level of performance, by comparison with the two optimized linear designs.

A summary of the performance metrics and design attributes, for the nonlinear and linear designs, is provided in Table 1. The cross-sectional areas (in.^{2}) for the optimized designs are reported next to each element, from which the different allocation of volume to the common load path between the nonlinear and linear designs is apparent. The

lateral force resistance of the nonlinear design, at a given displacement is marginally larger than that of the linear design and hence the total energy (E_T) absorbed up to the displacement constraint is larger for the nonlinear design by 1.4%. Moreover, the minimum and maximum cross-sectional areas of the nonlinear design, in comparison with the linear design, have been reduced.

When considering material inelasticity, the distribution of volume differs from the linear design, where some of the volume from the main load path in the base elements

|	Case 1	Case 2	Case 3	Case 4
v, in.^{3}	2.4241×10^4	2.4024×10^4	2.4674×10^4	2.4702×10^4
N	13	12	11	11
$\min(a)$, in.^{2}	1.98	0.93	6.89	6.92
$\max(a)$, in.^{2}	23.31	26.86	21.31	21.33

Fig. 7 Resulting nonlinear optimized designs for randomized starting cases for the 4×2 frame structure

Table 1 Summary of the performance metrics and design attributes of the nonlinear volume minimization optimized design and corresponding linear design for the 4 × 2 frame structure

	Nonlinear	Linear
	12.27 18.13 12.36 8.79 22.29 13.48 1.69 1.31 22.72 9.39 27.27	12.53 17.97 12.5 7.43 21.44 12.5 3.38 24.09 11.02 31.18
v, in.^{3}	2.3995×10^4	2.3995×10^4
d_v, in.	11.81	15.06
E_T, kips-in.	4.8863×10^3	4.8198×10^3
N	11	10
$\min(a)$, in.^{2}	1.31	3.38
$\max(a)$, in.^{2}	27.27	31.18

(i.e., 7 and 8) for the nonlinear design is reallocated to other elements in the primary load path (i.e., 5 and 6) and to add diagonal elements, or increase the volume of the common diagonal elements (i.e., 3 and 4). The redistribution is, in part, because in the nonlinear design the moment capacity of the elements is explicitly considered and if reached, supporting diagonal elements are required to limit deformations and hence additional elements appear where unbraced elements form plastic hinges, in particular at the connecting node of elements 9 and 10.

To illustrate the importance of the diagonal elements, element 3 is removed from the nonlinear design and an additional nonlinear analysis is performed for the same specified external force. The corresponding force-displacement response for the nonlinear design with and without element 3 is shown in Fig. 8. Although element 3 constitutes only 2.35% of the total volume of the
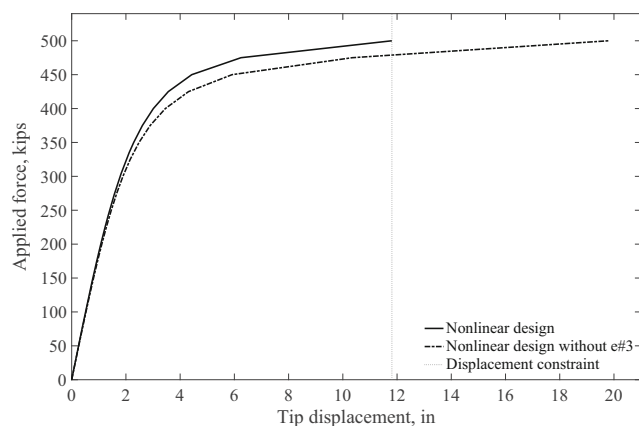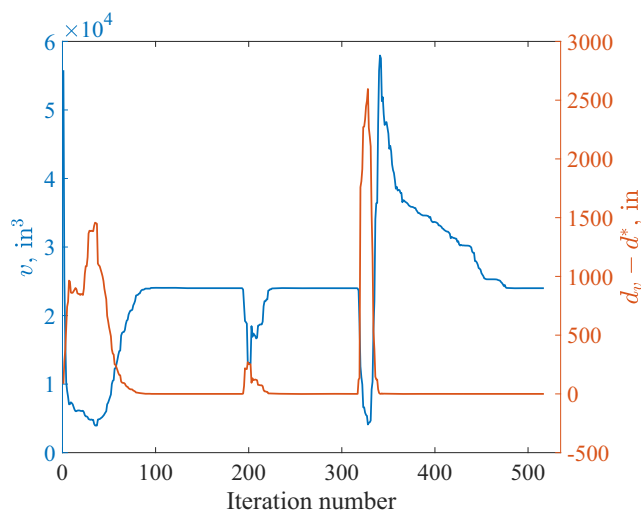
optimized structure, its importance in attaining the specified displacement constraint is significant, as its removal results in a substantial increase (68.6%) in tip displacement relative to the nonlinear design with element 3 intact and hence is not able to satisfy the displacement constraint.

The objective function and displacement constraint values for each iteration throughout the entire optimization process, following the procedure shown in Fig. 2, for the best nonlinear design of the 4 × 2 frame are shown in Fig. 9. The periodic drop and rise of the objective and constraint values correspond to the beginning of each phase of optimization. As can be seen from Fig. 9, the value of $d_v - d^*$ is approximately zero at the final phase, illustrating that the optimized nonlinear design satisfies the specified displacement constraint d^*.

Additionally, the hysteretic FE model permits assessing the cyclic response of the design and evaluating the inelastic displacements. The optimized nonlinear design was analyzed for the cyclic force history shown on the left side of Fig. 10 to obtain the system overall cyclic response shown in Fig. 10 and accordingly, the inelastic deformations can be evaluated.

3.2 Example 2: a 3 × 2 half beam

The second design example is a 3 × 2 half beam structure under a vertical external force at the center of the full domain. The beam domain, boundary conditions, and location of the applied force are shown in Fig. 11. Due to the symmetry of the boundary conditions and loading for the full domain, a symmetric design is expected, therefore half of the domain is modeled and used in the optimization process for computational efficiency. The dimensions of the

Fig. 8 Force-displacement responses of the optimized nonlinear design for 4 × 2 frame structure with and without element 3

Fig. 9 Iteration histories of the objective and constraint for the nonlinear design of 4 × 2 frame structure
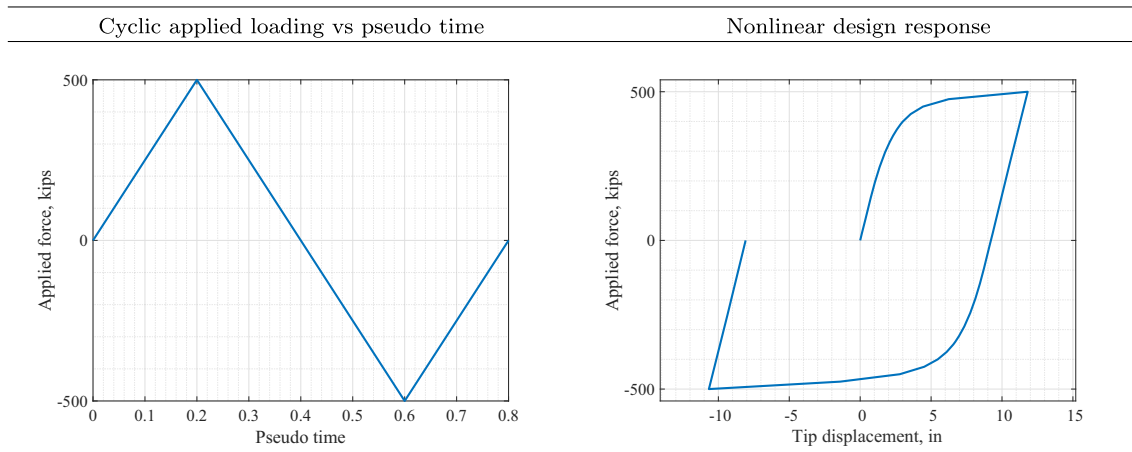
Fig. 10 Cyclic force history and cyclic response for the nonlinear design of 4×2 frame

domain are $L_x = 59.05$ ft (18 m) and $L_y = 19.68$ ft (6 m). Similar to Example 1, the nonlinear minimum volume design problem subject to displacement constraint is solved for a center displacement constraint as $d^* = L_x/200$ and applied external force of 250 kips.

As in Example 1, the values of the sensitivities for the displacement constraint evaluated using the analytical gradients developed for the hysteretic beam FE modeling approach via the direct differentiation method are compared with numerical sensitivities obtained by finite difference approximation for the 3×2 half beam ground structure. For comparison, these sensitivities are plotted in Fig. 12. As with Example 1, the sensitivities agree well with negligible relative error thus providing further verification of the accuracy of the analytical sensitivities obtained through the direct differentiation approach described in Section 2.2.2.
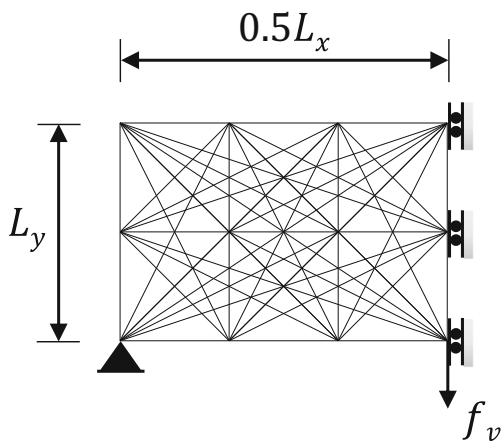
Similar to Example 1, the nonlinear design problem is solved for multiple starting cases, including uniform and randomized starting areas. The resulting optimized topologies for uniform and randomized areas are shown in Figs. 13 and 14, respectively. Plot of the randomized initial area values for each randomized starting case and design attributes are also presented in Fig. 14. Numerical values for the randomized areas for each starting case are tabulated and reported in Appendix 5. Again all designs satisfy the displacement constraint of $d^* = L_x/200 = 3.54$ in. so that by comparing the results shown in Fig. 13 with those shown in Fig. 14, the nonlinear design shown in Fig. 13 is comprised of the lowest volume and hence is considered the best nonlinear design solution.

Fig. 11 Ground structure for the 3×2 half beam structure under a vertical force
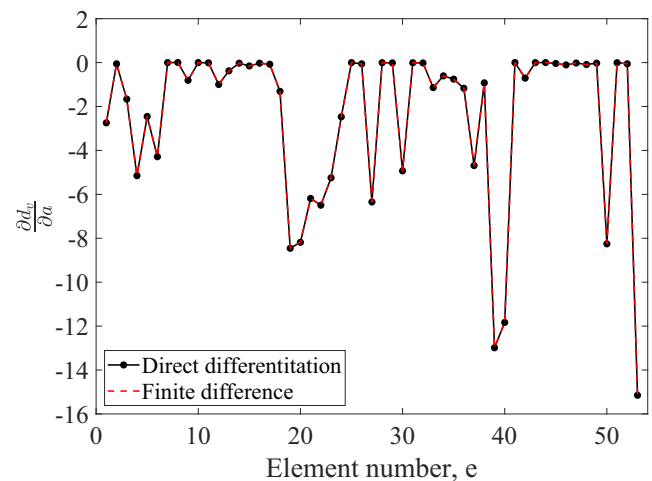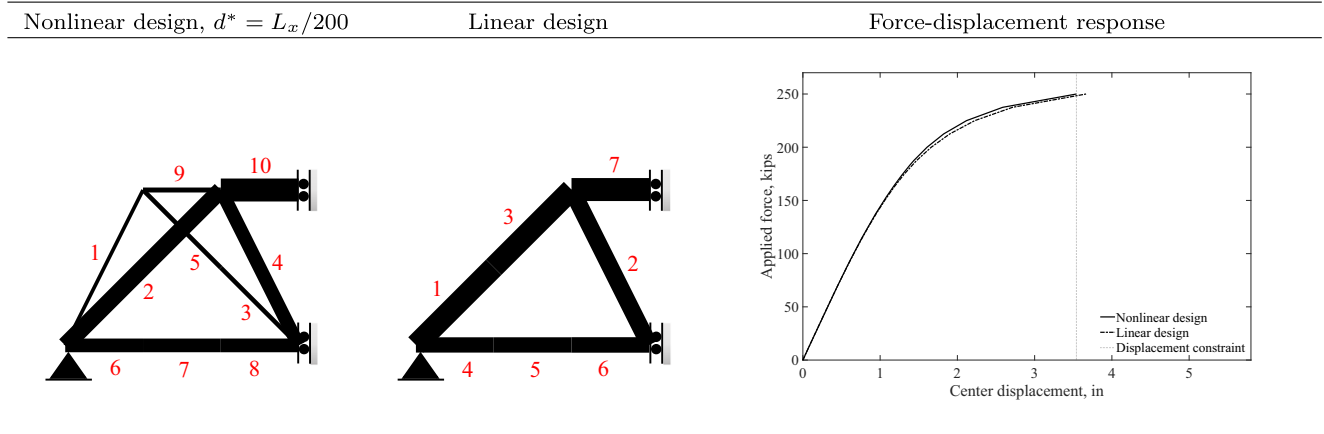

Fig. 12 Comparison of the results of sensitivity analysis derived with the analytical direct differentiation method and finite difference approximation for the 3×2 half beam ground structure

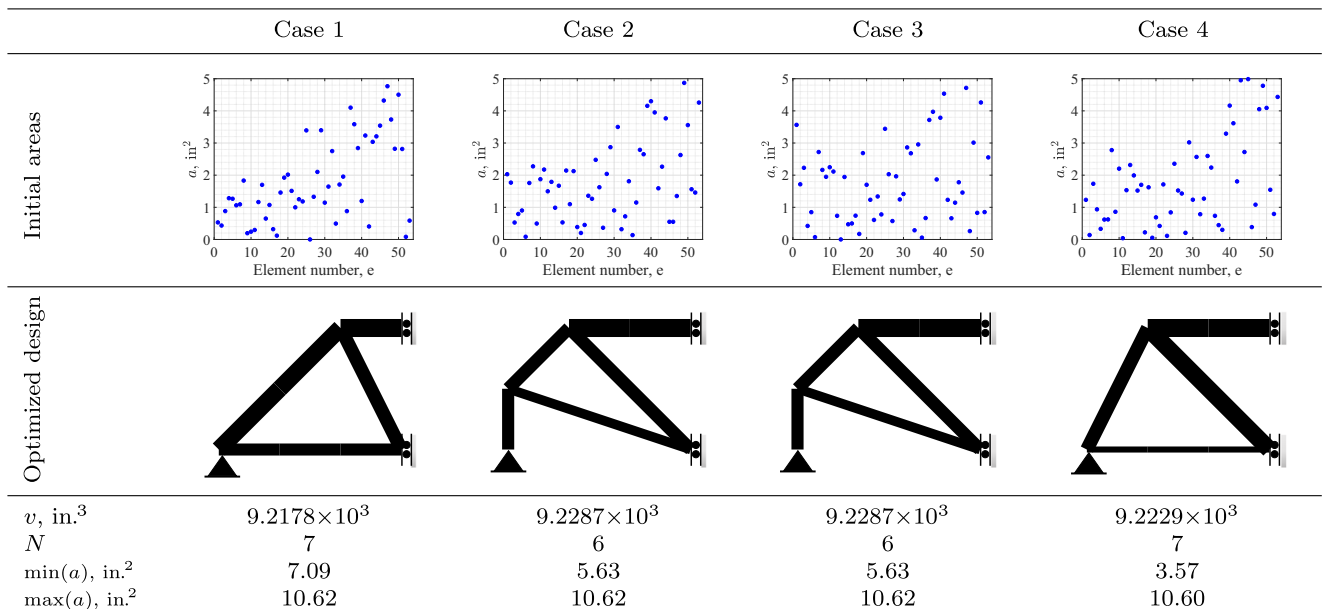| Nonlinear design, $d^* = L_x/200$	Linear design	Force-displacement response

Fig. 13 Nonlinear minimum volume design for $L_x/200$ center displacement and the comparative linear design with the equivalent volume for the 3×2 half beam structure along with the force-displacement responses for each optimized design. Numerical values adjacent to the elements indicate the element number

As with Example 1, the best nonlinear topology is compared with the optimized solutions from two linear topology optimization problems. Again a multistart strategy is employed for both linear topology optimization problems and the linear design reported for each optimization problem is the one with the lowest objective function value that satisfied the constraints from among all the starting cases. These linear design solutions where then evaluated using nonlinear FE analysis described in Section 2.2.1 to assess their respective performance and compare this performance to that of the best nonlinear design. The first linear optimization problem seeks to minimize the compliance for a given volume constraint.

More specifically, the linear design is obtained by setting the optimized volume of the nonlinear design as the volume constraint for the linear compliance problem for the purpose of comparison. The linear design and the associated force-displacement responses obtained from nonlinear quasi-static analysis of the nonlinear and linear designs are shown in Fig. 13. For reference the element with maximum area is located in the linear design solution (element 7). As seen from Fig. 13, the nonlinear topology obtained from the proposed methodology, shows a common primary load path with the linear design, but includes additional diagonal elements outside of this primary load path. Albeit by less of a margin than with Example 1, as expected, the

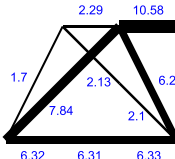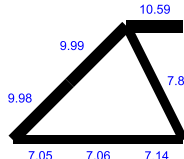|	Case 1	Case 2	Case 3	Case 4
v, in.^{3}	9.2178×10^3	9.2287×10^3	9.2287×10^3	9.2229×10^3
N	7	6	6	7
$\min(a)$, in.^{2}	7.09	5.63	5.63	3.57
$\max(a)$, in.^{2}	10.62	10.62	10.62	10.60

Fig. 14 Resulting nonlinear optimized designs for randomized starting cases for the 3×2 half beam structure
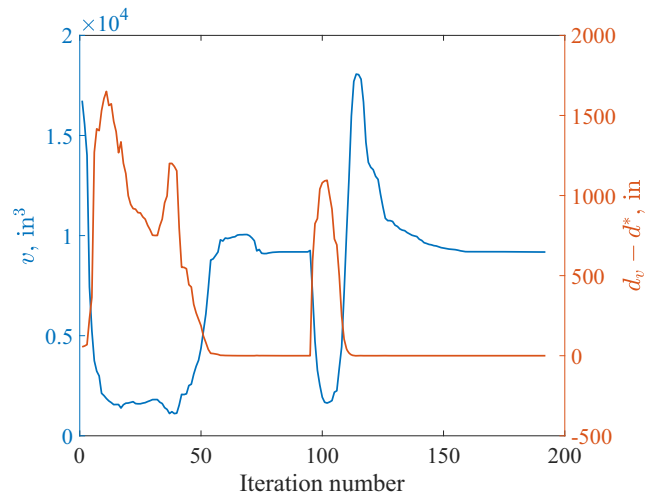
nonlinear design satisfies the specified center displacement constraint, whereas the linear design when evaluated by nonlinear FE analysis slightly exceeds the constraint for this example.

The second linear optimization problem seeks to minimize the volume subjected to a drift displacement constraint. Solving the linear volume minimization design problem subject to the displacement constraint d^* of $L_x/200$ resulted in a volume of 4.1016×10^3 in.^{3} (for details of the linear design problems, see Appendix 6). The topology for the linear volume minimization problem is similar to that shown in Fig. 13 and has been omitted to avoid unnecessary repetition. As expected, this volume is considerably smaller than the optimized volume of the nonlinear design. Scaling the linear volume by a factor of 2.25 results in a design, based on the linear volume minimization design, that satisfies the displacement constraint when evaluated by nonlinear quasi-static analysis. However, 2.25 times 4.1016×10^3 in.^{3}, or 9.2286×10^3 in.^{3}, that exceeds the volume of the nonlinear design of 9.1790×10^3 in.^{3}. These results are consistent with those observed for the nonlinear design of the 4×2 frame structure in Example 1, and again illustrate that the nonlinear design either offers better performance for the same volume or lower volume for a given level of performance, by comparison with the two linear designs.

Table 2 summarizes the results and attributes for the nonlinear and comparative linear design solutions for the 3×2 half beam. Again the cross-sectional areas (in.^{2}) for the optimized designs are reported next to each element, and the difference in the values of areas is shown. In the nonlinear design, the volume allocated to the primary load
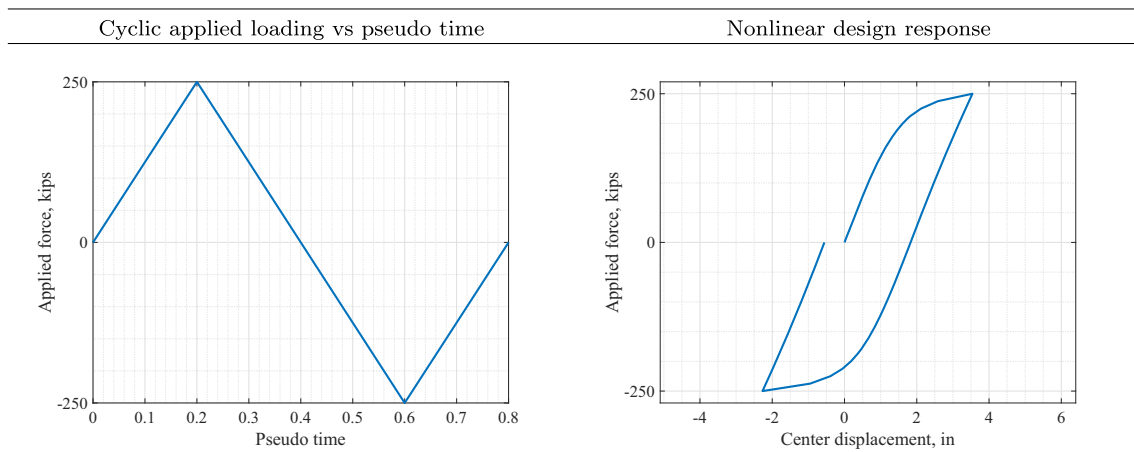

Fig. 15 Iteration histories of the objective and constraint for the nonlinear design of 3×2 half beam structure

path (i.e., elements 2, 4, 6, 7, 8, and 10) is less than for the linear design, and a portion of volume is allocated to the supplementary supporting elements (i.e., elements 1, 3, 5, and 9), which is necessary to satisfy the specified design constraint. Again, the nonlinear design has a marginally higher force resistance for a given displacement and as such results in a larger amount of absorbed energy (E_T) up to the displacement constraint, by comparison with the linear design, by 0.8%. In the nonlinear design, the minimum and maximum cross-sectional areas have been reduced relative to the linear design. Similar to Example 1, the optimized volume distribution and increase in the number of elements relative to the linear design are the main differentiating features.

The histories of the objective and displacement constraint for each iteration throughout the optimization process for the nonlinear design of the 3×2 half beam frame are shown in Fig. 15 following the process shown in Fig. 2. Again, in the final phase, that is, last iteration, the value of $d_v - d^*$ is approximately zero indicating that the displacement constraint is satisfied at the final stage of optimization. As with Example 1, the periodic drop and rise of the objective and constraint values correspond to the beginning of each phase of optimization.

As previously mentioned, the hysteretic FE modeling permits analysis of the cyclic response and evaluating the inelastic deformations of the system without any change in the formulation. For this example, the cyclic loading shown in Fig. 16 is applied to the optimized nonlinear beam design presented in Fig. 13 to obtain the cyclic response of the design and inelastic deformations.

Table 2 Summary of the performance metrics and design attributes of the nonlinear volume minimization optimized design and corresponding linear design for the 3×2 half beam structure

	Nonlinear	Linear
	(structure diagram: 2.29, 10.58, 1.7, 2.13, 6.23, 7.84, 2.1, 6.32, 6.31, 6.33)	*(structure diagram: 10.59, 9.99, 9.98, 7.88, 7.05, 7.06, 7.14)*
v, in.^{3}	9.1790×10^3	9.1790×10^3
d_v, in.	3.54	3.66
E_T, kips-in.	6.3150×10^2	6.2656×10^2
N	10	7
$\min(a)$, in.^{2}	1.70	7.05
$\max(a)$, in.^{2}	10.58	10.59

Fig. 16 Cyclic force history and cyclic response for the nonlinear design of 3 × 2 half beam

4 Summary and concluding remarks

This paper contributes a method for the topology optimization of nonlinear structures based on a hysteretic beam FE model. Two beneficial features of the hysteretic FE modeling approach in the context of topology optimization are that analytical sensitivities could be derived by invoking a mathematical approximation for the signum function and the stiffness and hysteretic matrices need only to be evaluated once for each nonlinear structural analysis. As such, original analytical sensitivities and solution algorithms were presented to combine the hysteretic FE modeling approach and topology optimization.

The utility of the method was demonstrated through two numerical design examples. The optimized designs are sought while permitting material inelasticity by way of inelastic deformations in individual elements. Due to the non-convexity of the optimization problem considered in this study, multiple starting cases with randomized initial cross-sectional areas were performed and used to initiate the optimization process. For each design example presented, the uniform area starting case resulted in the best nonlinear design solution. However, it is worth noting, that sampling from a high-dimensional design space subjected to nonlinear constraints in the context of topology optimization is an ongoing research topic. The resulting nonlinear design comprised of elements along a common load path similar to the comparative linear design. However, the distribution of volume to elements in the common load path varies and additional elements are included in the nonlinear design. These elements are necessary for the design to achieve the specified displacement constraint. While the primary structural system designs are similar, these differences between the nonlinear and linear designs serve important purposes in attaining the overall design objectives. Although the optimized design from the

nonlinear and linear designs share some similar features, in the context of frame structures and beam elements, the findings from this study suggest that the solution obtained from linear elastic problem formulation is not suitable if inelastic deformations are expected and that the inelastic deformations should be explicitly considered to ensure the designs compliance with the specified requirements.

For this study, the scope was restricted to planar frame structures composed of nonlinear Euler-Bernoulli beam elements to introduce the idea of hysteretic FE method for nonlinear topology optimization. As is well known, Newton type solution schemes require iterations at each step in the analysis that can significantly increase the computational cost relative to analysis of linear systems, as was observed for the numerical examples presented in this study. As such, part of ongoing research is aimed at devising a more efficient solution scheme for topology optimization employing the hysteretic finite element modeling approach. Other ongoing research is aimed at extending the suggested hysteretic FE topology optimization method to include nonlinear Timoshenko beam elements, local damage constraints, and time varying excitation for the design of frame structures whereby variation of the structural response with time is implicitly considered. Further extensions to 3D space frames and continuum structures are also possible and of interest to the authors in future work. Such extensions do however require enhancements to existing hysteretic FE beam models, including addition of transverse, rotation and torsion DOF and an appropriate yield function or development of a 3D hysteretic FE solid element.

Compliance with ethical standards

Appendix 1. Hysteretic forces and hysteretic capacities

The additional details for evaluation of the H_{1u}, $H_{1\phi}$, H_{2u} and $H_{2\phi}$ functions presented in Section 2.1 for the governing ODEs (7) are described in this section. First the hysteretic force ratios are defined as:

$$P_r = \frac{P^h}{P_c^h}, \quad M_r = \frac{M^h}{M_c^h}. \tag{32}$$

The hysteretic forces, P^h and M^h, and the hysteretic capacities, P_c^h and M_c^h, are defined using the following expressions:

$$P^h = (1 - \alpha_u)Eaz_u, \quad P_c^h = (1 - \alpha_u)a\sigma_y$$
$$M^h = (1 - \alpha_\phi)EIz_\phi, \quad M_c^h = (1 - \alpha_\phi)M_p, \tag{33}$$

where σ_y is the yield stress of the material. In (33), M_p stands for the plastic moment of a section, which mainly depends on the cross section type and its geometry. For the design examples considered in this paper, I-shaped sections are employed and M_p is evaluated using the following relations:

$$M_p = M_{pw} + M_{pf}, \quad M_{pw} = \sigma_y(h - 2t_f)^2 t_w/4$$
$$M_{pf} = \sigma_y t_f b_f (h - t_f), \tag{34}$$

where M_{pw} and M_{pf} are the plastic moments associated with web and flange of an I-shaped section, respectively. As shown in (34), section properties such as h (section depth), t_w (web thickness), t_f (flange thickness) and b_f (flange width) are required for M_p evaluation.

Appendix 2. Virtual work expression to obtain beam element stiffness and hysteretic matrices

As mentioned in Section 2.1, to derive the element stiffness and hysteretic matrices, proper shape functions should be used to interpolate the displacement and hysteretic fields in conjunction with the virtual work formulation. Following Triantafyllou and Koumousis (2012) and implementing the variational principle of virtual work, and then separating the elastic component from the hysteretic component, the following expression obtained as:

$$(\delta\mathbf{d}^{el})^T \int_0^L \mathbf{B}^T \mathbf{D} \mathbf{B} dx \cdot \mathbf{d}^{el} +$$
$$(\delta\mathbf{d}^{el})^T \int_0^L \mathbf{B}^T \mathbf{D}^h \mathbf{N}_z dx \cdot \mathbf{z}^{el} = (\delta\mathbf{d}^{e,l})^T \mathbf{f}^{el}, \tag{35}$$

where $\mathbf{B}$ is the strain-displacement matrix derived from shape functions of the Euler-Bernoulli beam element as follows:

$$\mathbf{B} = \begin{bmatrix} \frac{-1}{L} & 0 & 0 & \frac{-1}{L} & 0 & 0 \\ 0 & \frac{12x-6L}{L^3} & \frac{6xL-4L^2}{L^2} & 0 & \frac{-12x+6L}{L^3} & \frac{6xL-4L^2}{L^2} \end{bmatrix}^T, \tag{36}$$

and the matrices $\mathbf{D}$ and $\mathbf{D}^h$ are defined as:

$$\mathbf{D} = \begin{bmatrix} \alpha_u Ea & 0 \\ 0 & \alpha_\phi EI \end{bmatrix}, \quad \mathbf{D}^h = \begin{bmatrix} (1-\alpha_u)Ea & 0 \\ 0 & (1-\alpha_\phi)EI \end{bmatrix}. \tag{37}$$

Finally, matrix $\mathbf{N}_z$, representing the hysteretic interpolation functions in (35) is expressed as:

$$\mathbf{N}_z = \begin{bmatrix} 0.5 & 0 & 0.5 & 0 \\ 0 & 1 - \frac{x}{L} & 0 & \frac{x}{L} \end{bmatrix}. \tag{38}$$

The above expressions provide the details required to derive the element stiffness and hysteretic matrices.

Appendix 3. Derivation of $\mathbf{J}_{vn}$

As described in Section 2.2.1, the second part of the Jacobian matrix, is required and evaluated using:

$$\mathbf{J}_{vn} = \begin{bmatrix} \mathbf{0}_{(3r)\times(3r+4N)} \\ \mathbf{J}_d \quad \mathbf{J}_z \end{bmatrix}, \tag{39}$$

where the matrices $\mathbf{J}_d$ and $\mathbf{J}_z$ are the assembly of the following vectors evaluated at each node, which results in a 2×2 matrix for each element:

$$\mathbf{j}_z^e = \begin{bmatrix} \frac{\partial H_{1u}}{\partial z_u} H_{2u} + H_{1u} \frac{\partial H_{2u}}{\partial z_u} & 0 \\ 0 & \frac{\partial H_{1\phi}}{\partial z_\phi} H_{2\phi} + H_{1\phi} \frac{\partial H_{2\phi}}{\partial z_\phi} \end{bmatrix} \Delta\boldsymbol{\epsilon}$$

$$\mathbf{j}_d^e = \begin{bmatrix} H_{1u} \frac{\partial H_{2u}}{\partial u} & 0 \\ 0 & H_{1\phi} \frac{\partial H_{2\phi}}{\partial \theta} \end{bmatrix} \Delta\boldsymbol{\epsilon}, \tag{40}$$

where as defined previously, $\Delta\boldsymbol{\epsilon} = \boldsymbol{\epsilon}_{i+1}^j - \boldsymbol{\epsilon}_i$. The derivative components in (40), are obtained by differentiation of the H_{1u}, $H_{1\phi}$, H_{2u} and $H_{2\phi}$ functions with respect to

displacement and hysteretic DOF, yielding the following expressions:

$$\frac{\partial H_{1u}}{\partial z_u} = n|P_r|^{n-1}\text{sign}(P_r)(1-\alpha_u)Ea/P_c^h$$

$$\frac{\partial H_{1\phi}}{\partial z_\phi} = n|M_r|^{n-1}\text{sign}(M_r)(1-\alpha_\phi)EI/M_c^h$$

$$\frac{\partial H_{2u}}{\partial z_u} = \gamma\zeta(1-\alpha_u)Ea\Delta\epsilon_u\text{sech}(\zeta P^h\Delta\epsilon_u)^2$$

$$\frac{\partial H_{2\phi}}{\partial z_\phi} = \gamma\zeta(1-\alpha_\phi)EI\Delta\epsilon_\phi\text{sech}(\zeta M^h\Delta\epsilon_\phi)^2$$

$$\frac{\partial H_{2u}}{\partial u} = \gamma\zeta\left(P^h\frac{\partial\Delta\epsilon_u}{\partial u}\right)\text{sech}(\zeta P^h\Delta\epsilon_u)^2$$

$$\frac{\partial H_{2\phi}}{\partial\theta} = \gamma\zeta\left(M^h\frac{\partial\Delta\epsilon_\phi}{\partial\theta}\right)\text{sech}(\zeta M^h\Delta\epsilon_\phi)^2. \qquad (41)$$

Note, assigning an even value to n, removes the absolute value operator from the H_{1u}, $H_{1\phi}$ and their derivatives, resulting in a smooth functions without introducing discontinuity in sensitivities.

Appendix 4. Sensitivities

In this section, necessary details of sensitivity analysis described in Section 2.2.2, are presented. First, the derivatives for functions H_{1u}, $H_{1\phi}$, H_{2u}, and $H_{2\phi}$ with respect to design variable, a, are obtained by differentiation of (4) and (14):

$$\frac{\partial H_{1u}}{\partial a} = n|P_r|^{n-1}\text{sign}(P_r)\frac{\partial P_r}{\partial a}$$

$$\frac{\partial H_{1\phi}}{\partial a} = n|M_r|^{n-1}\text{sign}(M_r)\frac{\partial M_r}{\partial a}$$

$$\frac{\partial H_{2u}}{\partial a} = \gamma\zeta\left(\frac{\partial P^h}{\partial a}\Delta\epsilon_u + P^h\frac{\partial\Delta\epsilon_u}{\partial a}\right)\text{sech}(\zeta P^h\Delta\epsilon_u)^2$$

$$\frac{\partial H_{2\phi}}{\partial a} = \gamma\zeta\left(\frac{\partial M^h}{\partial a}\Delta\epsilon_\phi + M^h\frac{\partial\Delta\epsilon_\phi}{\partial a}\right)\text{sech}(\zeta M^h\Delta\epsilon_\phi)^2. \qquad (42)$$

The terms $\partial P_r/\partial a$ and $\partial M_r/\partial a$ in (42) are expressed as:

$$\frac{\partial P_r}{\partial a} = \frac{\frac{\partial P^h}{\partial a}P_c^h - P^h\frac{\partial P_c^h}{\partial a}}{(P_c^h)^2}$$

$$\frac{\partial M_r}{\partial a} = \frac{\frac{\partial M^h}{\partial a}M_c^h - M^h\frac{\partial M_c^h}{\partial a}}{(M_c^h)^2}, \qquad (43)$$

where the derivatives of P^h, P_c^h, M^h, and M_c^h with respect to design variables are obtained by differentiation of (33):

$$\frac{\partial P^h}{\partial a} = (1-\alpha_u)\left(Ez_u + Ea\frac{\partial z_u}{\partial a}\right)$$

$$\frac{\partial P_c^h}{\partial a} = (1-\alpha_u)\sigma_y$$

$$\frac{\partial M^h}{\partial a} = (1-\alpha_\phi)\left(E\frac{\partial I}{\partial a}z_\phi + EI\frac{\partial z_\phi}{\partial a}\right)$$

$$\frac{\partial M_c^h}{\partial a} = (1-\alpha_\phi)\frac{\partial M_p}{\partial a}, \qquad (44)$$

and the $\partial M_p/\partial a$ term is evaluated by differentiating (34) as follows:

$$\frac{\partial M_p}{\partial a} = \frac{\partial M_{pw}}{\partial a} + \frac{\partial M_{pf}}{\partial a}$$

$$\frac{\partial M_{pw}}{\partial a} = \sigma_y\left(\frac{\partial t_w}{\partial a}(h-2t_f)^2/4 + t_w(h-2t_f)\right.$$

$$\left. \times\left(\frac{\partial h}{\partial a} - 2\frac{\partial t_f}{\partial a}\right)/2\right)$$

$$\frac{\partial M_{pf}}{\partial a} = \sigma_y\left(\frac{\partial t_f}{\partial a}b_f(h-t_f) + t_f\frac{\partial b_f}{\partial a}(h-t_f)\right.$$

$$\left. + t_fb_f\left(\frac{\partial h}{\partial a} - \frac{\partial t_f}{\partial a}\right)\right). \qquad (45)$$

The derivative for $\partial\mathbf{J}_{vn}/\partial a$ is expressed using:

$$\frac{\partial\mathbf{J}_{vn}}{\partial a} = \begin{bmatrix} \mathbf{0}_{(3r)\times(3r+4N)} \\ \frac{\partial\mathbf{J}_d}{\partial a} & \frac{\partial\mathbf{J}_z}{\partial a} \end{bmatrix}, \qquad (46)$$

where $\partial\mathbf{J}_z/\partial a$, is the global assembly of the following element-level expression obtained by differentiating (40):

$$\frac{\partial\mathbf{j}_z^e}{\partial a} = \left[\begin{matrix} \frac{\partial^2 H_{1u}}{\partial a\partial z_u}H_{2u} + \frac{\partial H_{1u}}{\partial z_u}\frac{\partial H_{2u}}{\partial a} + \frac{\partial H_{1u}}{\partial a}\frac{\partial H_{2u}}{\partial z_u} + H_{1u}\frac{\partial^2 H_{2u}}{\partial a\partial z_u} \\ 0 \\ 0 \\ \frac{\partial^2 H_{1\phi}}{\partial a\partial z_\phi}H_{2\phi} + \frac{\partial H_{1\phi}}{\partial z_\phi}\frac{\partial H_{2\phi}}{\partial a} + \frac{\partial H_{1\phi}}{\partial a}\frac{\partial H_{2\phi}}{\partial z_\phi} + H_{1\phi}\frac{\partial^2 H_{2\phi}}{\partial a\partial z_\phi} \end{matrix}\right]\Delta\epsilon$$

$$+ \left[\begin{matrix} \frac{\partial H_{1u}}{\partial z_u}H_{2u} + H_{1u}\frac{\partial H_{2u}}{\partial z_u} & 0 \\ 0 & \frac{\partial H_{1\phi}}{\partial z_\phi}H_{2\phi} + H_{1\phi}\frac{\partial H_{1\phi}}{\partial z_\phi} \end{matrix}\right]\frac{\partial\Delta\epsilon}{\partial a}, \qquad (47)$$

and similarly for the $\partial\mathbf{J}_d/\partial a$, the element-level expression is obtained by differentiating (40):

$$\frac{\partial\mathbf{j}_d^e}{\partial a} = \left[\begin{matrix} \frac{\partial H_{1u}}{\partial a}\frac{\partial H_{2u}}{\partial u} + H_{1u}\frac{\partial^2 H_{2u}}{\partial a\partial u} & 0 \\ 0 & \frac{\partial H_{1\phi}}{\partial a}\frac{\partial H_{2\phi}}{\partial\theta} + H_{1\phi}\frac{\partial^2 H_{2\phi}}{\partial a\partial\theta} \end{matrix}\right]\Delta\epsilon$$

$$+ \left[\begin{matrix} H_{1u}\frac{\partial H_{2u}}{\partial u} & 0 \\ 0 & H_{1\phi}\frac{\partial H_{2\phi}}{\partial\theta} \end{matrix}\right]\frac{\partial\Delta\epsilon}{\partial a}. \qquad (48)$$

As indicated by (47) and (48), the sensitivities of the functions presented in (41) with respect to design variables

are required, where the derivation results in the following expressions:

$$\frac{\partial^2 H_{1u}}{\partial a \partial z_u} = n(1-\alpha_u)E(n-1)\frac{\partial P_r}{\partial a}|P_r|^{n-2}\mathrm{sign}(P_r)a/P_u^h$$

$$\frac{\partial^2 H_{1\phi}}{\partial a \partial z_\phi} = n(1-\alpha_\phi)E\left((n-1)\frac{\partial M_r}{\partial a}|M_r|^{n-2}\mathrm{sign}(M_r)I/M_y^h\right.$$
$$\left.+|M_r|^{n-1}\frac{\frac{\partial I}{\partial a}M_y^h - I\frac{\partial M_y^h}{\partial a}}{(M_y^h)^2}\right)$$

$$\frac{\partial^2 H_{2u}}{\partial a \partial z_u} = (1-\alpha_u)E\gamma\zeta\,\mathrm{sech}(\zeta P^h \Delta\epsilon_u{}^e)^2\left(\Delta\epsilon_u + a\frac{\partial \Delta\epsilon_u}{\partial a}\right.$$
$$\left.-2a\Delta\epsilon_u\tanh(\zeta P^h \Delta\epsilon_u{}^e)\left(\frac{\partial P^h}{\partial a}\Delta\epsilon_u + P^h\frac{\partial \Delta\epsilon_u}{\partial a}\right)\right)$$

$$\frac{\partial^2 H_{2\phi}}{\partial a \partial z_\phi} = (1-\alpha_\phi)E\gamma\zeta\,\mathrm{sech}(\zeta M^h \Delta\epsilon_\phi)^2$$
$$\times\left(\frac{\partial I}{\partial a}\Delta\epsilon_\phi + I\frac{\partial \Delta\epsilon_\phi}{\partial a} - 2I\Delta\epsilon_\phi\tanh(\zeta P^h \Delta\epsilon_\phi)\right.$$
$$\left.\times\left(\frac{\partial M^h}{\partial a}\Delta\phi + M^h\frac{\partial \Delta\epsilon_\phi}{\partial a}\right)\right)$$

$$\frac{\partial^2 H_{2u}}{\partial a \partial u} = \gamma\zeta\,\mathrm{sech}(\zeta P^h \Delta\epsilon_u)^2\left(\frac{\partial P^h}{\partial a}\frac{\partial \epsilon_u}{\partial u} + P^h\frac{\partial^2 \epsilon_u}{\partial a \partial u}\right.$$
$$\left.-2\zeta P^h\frac{\partial \Delta\epsilon_u}{\partial u}\tanh(\zeta P^h \Delta\epsilon_u)\left(\frac{\partial P^h}{\partial a}\Delta\epsilon_u + P^h\frac{\partial \Delta\epsilon_u}{\partial a}\right)\right)$$

$$\frac{\partial^2 H_{2\phi}}{\partial a \partial \theta} = \gamma\zeta\,\mathrm{sech}(\zeta M^h \Delta\epsilon_\phi)^2\left(\frac{\partial M^h}{\partial a}\frac{\partial \Delta\epsilon_\phi}{\partial \theta} + M^h\frac{\partial^2 \Delta\epsilon_\phi}{\partial a \partial \theta}\right.$$
$$\left.-2\zeta M^h\frac{\partial \Delta\epsilon_\phi}{\partial \theta}\tanh(\zeta M^h \Delta\epsilon_\phi)\left(\frac{\partial M^h}{\partial a}\Delta\epsilon_\phi + M^h\frac{\partial \Delta\epsilon_\phi}{\partial a}\right)\right). \tag{49}$$

Last, the matrices $\partial \mathbf{K}/\partial a$ and $\partial \mathbf{H}/\partial a$, are the global assembly of the element derivative matrices according to:

$$\frac{\partial \mathbf{K}^e}{\partial a} = \boldsymbol{\Lambda}^T\frac{\partial \mathbf{K}^{el}}{\partial a}\boldsymbol{\Lambda}, \quad \frac{\partial \mathbf{H}^e}{\partial a} = \boldsymbol{\Lambda}^T\frac{\partial \mathbf{H}^{el}}{\partial a}, \tag{50}$$

where the matrices $\partial \mathbf{K}^{el}/\partial a$ and $\partial \mathbf{H}^{el}/\partial a$ are obtained through differentiating (10).

$$\frac{\partial \mathbf{K}^{el}}{\partial a} = E\begin{bmatrix} \frac{\alpha_u}{L} & 0 & 0 & \frac{-\alpha_u}{L} & 0 & 0 \\ 0 & \frac{12\frac{\partial I}{\partial a}\alpha_\phi}{L^3} & \frac{6\frac{\partial I}{\partial a}\alpha_\phi}{L^2} & 0 & -\frac{12\frac{\partial I}{\partial a}\alpha_\phi}{L^3} & \frac{6\frac{\partial I}{\partial a}\alpha_\phi}{L^2} \\ 0 & \frac{6\frac{\partial I}{\partial a}\alpha_\phi}{L^2} & \frac{4\frac{\partial I}{\partial a}\alpha_\phi}{L} & 0 & -\frac{6\frac{\partial I}{\partial a}\alpha_\phi}{L^2} & \frac{2EI\alpha_\phi}{L} \\ \frac{-\alpha_u}{L} & 0 & 0 & \frac{\alpha_u}{L} & 0 & 0 \\ 0 & -\frac{12\frac{\partial I}{\partial a}\alpha_\phi}{L^3} & -\frac{6\frac{\partial I}{\partial a}\alpha_\phi}{L^2} & 0 & \frac{12\frac{\partial I}{\partial a}\alpha_\phi}{L^3} & -\frac{6\frac{\partial I}{\partial a}\alpha_\phi}{L^2} \\ 0 & \frac{6\frac{\partial I}{\partial a}\alpha_\phi}{L^2} & \frac{2\frac{\partial I}{\partial a}\alpha_\phi}{L} & 0 & -\frac{6\frac{\partial I}{\partial a}\alpha_\phi}{L^2} & \frac{4\frac{\partial I}{\partial a}\alpha_\phi}{L} \end{bmatrix}$$

$$\frac{\partial \mathbf{H}^{el}}{\partial a} = E\begin{bmatrix} \frac{(\alpha_u-1)}{2} & 0 & \frac{(\alpha_u-1)}{2} & 0 \\ 0 & \frac{\frac{\partial I}{\partial a}(\alpha_\phi-1)}{L} & 0 & -\frac{\frac{\partial I}{\partial a}(\alpha_\phi-1)}{L} \\ 0 & \frac{\partial I}{\partial a}(\alpha_\phi-1) & 0 & 0 \\ -\frac{(\alpha_u-1)}{2} & 0 & -\frac{(\alpha_u-1)}{2} & 0 \\ 0 & -\frac{\frac{\partial I}{\partial a}(\alpha_\phi-1)}{L} & 0 & \frac{\frac{\partial I}{\partial a}(\alpha_\phi-1)}{L} \\ 0 & 0 & 0 & -\frac{\partial I}{\partial a}(\alpha_\phi-1) \end{bmatrix}, \tag{51}$$

that completes the derivations for the sensitivities. The derivatives of section properties such as $\partial I/\partial a$ and $\partial h/\partial a$

for I-shaped cross sections are adopted from Changizi and Jalalpour (2017b).

Appendix 5. Cross-sectional areas for randomized starting cases

As described in Sections 2.3 and 3, a multi-start strategy is performed in an attempt seeking the global optima. The specific values of areas for each randomized starting cases of 4 × 2 frame and 3 × 2 half beam ground structures for the nonlinear design problem are tabulated in Tables 3 and 4, respectively. The element numbering is generally defined in a way that the elements connected to each node are concatenated in the global element connectivity matrix. Node numbering starts from the left bottom, row-wise, of the domain and continues to the node on the top right.

Table 3 Values of cross-sectional areas (in.^{2}) for the randomized starting cases of the 4 × 2 frame ground structure

Element number	Case 1	Case 2	Case 3	Case 4
1	8.0706	0.9619	3.2358	2.8014
2	4.0199	0.35266	3.2957	0.83283
3	3.1768	2.2437	3.0726	1.689
4	0.83349	1.9658	2.2373	1.5995
5	0.85705	1.4345	1.0385	0.38898
6	0.27421	2.626	0.82324	0.18225
7	8.2593	5.5058	3.8126	0.80693
8	6.3876	6.7692	1.9223	1.2549
9	3.1885	5.1734	4.295	0.65097
10	1.7917	5.3946	5.2648	2.1031
11	0.67181	0.75303	0.11323	0.082275
12	2.5162	0.54459	2.0223	0.95027
13	8.9293	6.1053	0.73508	0.58404
14	0.97425	0.52031	4.2824	1.9011
15	1.4736	2.9138	5.281	0.37995
16	1.7932	2.3252	0.28257	0.90026
17	0.29909	3.3769	3.5465	1.6023
18	2.4252	1.6676	0.060188	0.49979
19	3.6369	3.4501	5.7728	0.16879
20	5.6182	3.7236	4.1844	0.48448
21	2.299	4.1109	2.8518	0.90211
22	2.8049	2.2801	3.737	0.59814
23	0.62398	1.3635	3.394	0.36814
24	1.3519	0.51589	2.0725	1.3164
25	1.4564	5.1392	1.1638	2.4494
26	6.8521	2.2987	1.8386	3.4494
27	4.9796	0.24653	0.97245	0.99311
28	2.0052	4.1867	0.22328	2.1322
29	2.771	0.95207	0.40373	0.0093546

Table 3 (continued)

Element number	Case 1	Case 2	Case 3	Case 4
30	1.189	1.7349	2.3272	0.97855
31	4.796	6.0311	7.9323	2.8721
32	4.7584	1.9922	1.8924	0.52829
33	3.4155	4.0836	2.1923	2.1144
34	1.5153	1.7305	4.1548	1.3682
35	1.2095	2.68	3.5698	1.3251
36	1.6045	2.4215	2.2404	0.80644
37	3.82	3.8784	8.343	2.8416
38	2.0556	0.10857	4.0941	0.74611
39	3.1916	1.8349	1.7976	0.5067
40	3.3557	1.8603	2.7958	0.55999
41	3.8353	2.3699	2.0612	2.0957
42	3.8807	1.7279	2.4946	2.9755
43	0.71382	4.5571	3.6315	0.65863
44	0.13967	2.3843	2.8182	0.9128
45	2.6228	7.7846	3.4745	3.0907
46	1.8151	2.1694	3.2175	1.3939
47	3.7367	4.2653	4.007	2.2475
48	4.3246	1.7397	2.463	0.36516
49	8.4575	7.0896	4.6581	2.9658
50	2.6174	4.1875	3.1157	1.5325
51	2.1735	3.3093	4.3206	0.89255
52	6.9044	1.8942	0.69722	1.7058
53	6.8631	6.9308	6.0744	1.4308
54	4.2338	5.2646	5.3185	1.3592
55	9.506	4.0621	4.2326	4.0589
56	1.3539	8.3242	1.595	0.53273
57	8.7118	5.4395	4.136	4.165
58	5.9215	0.336 1	0.584	4.2646
59	2.7119	9.5344	5.4283	1.7975
60	1.2593	2.0741	4.9356	2.1806
61	0.527	0.689	2.5994	2.9014
62	2.237	2.275	1.5001	3.5534
63	2.0908	6.3792	3.6879	3.7646
64	8.5128	0.966	8.6685	3.8427
65	1.432	7.292	9.3462	1.973
66	6.6027	1.919	8.2827	2.1767
67	8.9821	2.4785	0.11702	4.849
68	1.9632	5.0466	0.067	2.9052
69	2.187	9.2845	1.011	4.3084
70	6.9137	0.238	9.2039	1.4012
71	8.6885	9.7961	0.50929	3.1554
72	0.46736	3.9499	4.5149	2.9832
73	0.343	6.6228	8.4087	4.8851
74	9.569	1.1155	8.7092	0.43555

Table 4 Values of cross-sectional areas (in.^{2}) for the randomized starting cases of the 3×2 half beam ground structure

Element number	Case 1	Case 2	Case 3	Case 4
1	0.53091	2.0298	3.5643	1.2329
2	0.43366	1.7685	1.7167	0.1382
3	0.883	0.52707	2.2287	1.7326
4	1.2843	0.79316	0.42191	0.93694
5	1.2667	0.90156	0.84956	0.33059
6	1.063	0.085274	0.07251	0.61955
7	1.0928	1.7572	2.7203	0.62374
8	1.8322	2.2743	2.1636	2.7794
9	0.19517	0.49549	1.9484	0.8614
10	0.24238	1.8745	2.2464	2.2025
11	0.29572	2.1746	2.1128	0.040158
12	1.1641	1.4984	0.73591	1.5327
13	1.6988	1.7916	0.0012272	2.3168
14	0.65084	0.98742	1.944	1.992
15	1.074	1.6719	0.47219	1.5212
16	0.32028	0.53057	0.49845	1.6992
17	0.11928	2.1438	0.74059	0.22096
18	1.4593	1.0981	0.17242	1.6224
19	1.9231	2.1254	2.6867	0.053104
20	2.017	0.38652	1.7014	0.68823
21	1.5116	0.20232	1.235	0.42074
22	0.99969	0.45191	0.60764	1.7125
23	1.251	1.3595	1.3378	0.11274
24	1.1828	1.2653	0.77897	0.84275
25	3.3927	2.4772	3.4415	2.3559
26	0.0011334	1.6239	2.0295	1.523
27	1.3278	0.36402	0.57301	1.4297
28	2.1015	2.0397	1.9638	0.20689
29	3.3962	2.8702	1.246	3.0203
30	1.1449	0.90435	1.4157	1.2369
31	1.6451	3.4998	2.8631	2.5674
32	2.7492	0.31866	2.6807	0.78537
33	0.49437	0.7187	0.28536	1.2705
34	1.7088	1.8108	2.9557	2.5976
35	1.9546	0.13572	0.057169	2.2366
36	0.88168	1.1491	0.66612	0.73509
37	4.1006	2.7869	3.7176	0.44655
38	3.5837	2.6507	3.9716	0.29984
39	2.8431	4.156	1.8668	3.2915
40	1.1971	4.3001	3.786	4.1633
41	3.2333	3.9509	4.5352	3.6143
42	0.40504	1.5915	1.2331	1.8056
43	3.037	2.2644	0.65871	4.951
44	3.2067	3.7667	1.144	2.7201
45	3.5406	0.55012	1.779	4.9876
46	4.3217	0.54952	1.4592	0.38484

Table 4   (continued)

Element number	Case 1	Case 2	Case 3	Case 4
47	4.7659	1.3514	4.7142	1.0826
48	3.7311	2.627	0.26082	4.0527
49	2.821	4.8704	3.0124	4.7804
50	4.504	3.5573	0.82798	4.092
51	2.8145	1.5616	4.2614	1.5454
52	0.082397	1.4594	0.85168	0.79402
53	0.58638	4.258	2.5526	4.4338

Appendix 6. Linear topology optimization design problems

As mentioned in Section 3, two linear design problems are solved to investigate optimality of the nonlinear designs and compare the optimized topologies. The first is solved with the optimal volume obtained from the nonlinear design as a constraint, where the compliance is set as the objective to find the most stiff structure for a given volume. This design problem is expressed as:

$$
\begin{aligned}
\text{Find}: \quad & a_1, ..., a_N \\
\underset{\mathbf{a}}{\text{Minimize}}: \quad & c = \mathbf{f}^T \mathbf{d} \\
\text{Subject to}: \quad & \mathbf{Kd} = \mathbf{f} \\
& v = \sum_{s=1}^{N} a_s L_s \leq v_{opt} \\
& 0 < \rho_{\min} < a \leq \rho_{\max},
\end{aligned}
\tag{52}
$$

where linear equilibrium equation, volume and bounds on cross-sectional areas are imposed as the constraints (more information can be found in Changizi and Jalalpour (2017a)). The second linear design problem is analogous to the nonlinear design problem, where the goal is to minimize the volume of the structural system subject to equilibrium and displacement constraint, stated as:

$$
\begin{aligned}
\text{Find}: \quad & a_1, ..., a_N \\
\underset{\mathbf{a}}{\text{Minimize}}: \quad & v = \sum_{s=1}^{N} a_s L_s \\
\text{Subject to}: \quad & \mathbf{Kd} = \mathbf{f} \\
& d_v \leq d^* \\
& 0 < \rho_{\min} < a \leq \rho_{\max},
\end{aligned}
\tag{53}
$$

where linear equilibrium equation, displacement constraint and bounds on cross-sectional areas are imposed as the constraints. For both linear design problems, the stiffness matrix is assembled through element-level matrix shown in (10) by setting α_u and α_b to 1.

References

Achtziger W, Bendsøe MP (1995) Design for maximal flexibility as a simple computational model of damage. Struct Optim 10(3–4):258–268

Alberdi R, Khandelwal K (2017) Topology optimization of pressure dependent elastoplastic energy absorbing structures with material damage constraints. Finite Elem Anal Des 133:42–61

Alberdi R, Zhang G, Li L, Khandelwal K (2018) A unified framework for nonlinear path-dependent sensitivity analysis in topology optimization. Int J Numer Methods Eng, vol 115

American Institute of Steel Construction (2015) Steel construction manual shapes database

Amir M, Papakonstantinou K, Warn G (2019) A consistent timoshenko hysteretic beam finite element model. Int J Non-Linear Mech, vol 119

Asadpoure A, Tootkaboni M, Guest JK (2011) Robust topology optimization of structures with uncertainties in stiffness–application to truss structures. Comput Struct 89(11):1131–1141

ASCE (2017) Minimum design loads for buildings and other structures. American Society of Civil Engineers, Reston, asce/sei 7–16 edition

Baber TT, Noori MN (1985) Random vibration of degrading, pinching systems. J Eng Mech 111(8):1010–1026

Baber TT, Wen Y-K (1981) Random vibration hysteretic, degrading systems. J Eng Mech Div 107(6):1069–1087

Bathe K-J (2006) Finite element procedures. Klaus-Jurgen Bathe

Bendsoe MP, Sigmund O (2004) Topology optimization: theory, methods and applications. Springer, Berlin

Boese KD, Kahng AB, Muddu S (1994) A new adaptive multi-start technique for combinatorial global optimizations. Oper Res Lett 16(2):101–114

Bouc R (1967) Forced vibration of mechanical systems with hysteresis. In: Proceedings of the fourth conference on non-linear oscillation. Prague, p 315

Casciati F (1989) Stochastic dynamics of hysteretic media. Struct Saf 6(2–4):259–269

Changizi N, Jalalpour M (2017a) Robust topology optimization of frame structures under geometric or material properties uncertainties. Struct Multidiscip Optim 56(4):791–807

Changizi N, Jalalpour M (2017b) Stress-based topology optimization of steel-frame structures using members with standard cross sections: gradient-based approach. J Struct Eng 143(8):04017078

Deaton JD, Grandhi RV (2014) A survey of structural and multidisciplinary continuum topology optimization: post 2000. Struct Multidiscip Optim 49(1):1–38

Erlicher S, Point N (2004) Thermodynamic admissibility of Bouc–Wen type hysteresis models. C R Mec 332(1):51–57

Foliente GC (1995) Hysteresis modeling of wood joints and structural systems. J Struct Eng 121(6):1013–1022

Gömöry F, Vojenčiak M, Pardo E, Šouc J (2009) Magnetic flux penetration and AC loss in a composite superconducting wire with ferromagnetic parts. Supercond Sci Technol 22(3):034017

James KA, Waisman H (2014) Failure mitigation in optimal topology design using a coupled nonlinear continuum damage model. Comput Methods Appl Mech Eng 268:614–631

James KA, Waisman H (2015) Topology optimization of structures under variable loading using a damage superposition approach. Int J Numer Methods Eng 101(5):375–406

Kim T, Rook T, Singh R (2003) Effect of smoothening functions on the frequency response of an oscillator with clearance non-linearity. J Sound Vib 263(3):665–678

Klarbring A, Strömberg N (2013) Topology optimization of hyperelastic bodies including non-zero prescribed displacements. Struct Multidiscip Optim 47(1):37–48

Kleiber M (1993) Shape and non-shape structural sensitivity analysis for problems with any material and kinematic non-linearity. Comput Methods Appl Mech Eng 108(1–2):73–97

Le C, Norato J, Bruns T, Ha C, Tortorelli D (2010) Stress-based topology optimization for continua. Struct Multidiscip Optim 41(4):605–620

Li L, Khandelwal K (2017) Topology optimization of geometrically nonlinear trusses with spurious eigenmodes control. Eng Struct 131:324–344

Li L, Zhang G, Khandelwal K (2017) Design of energy dissipating elastoplastic structures under cyclic loads using topology optimization. Struct Multidiscip Optim 56(2):391–412

Li L, Zhang G, Khandelwal K (2018) Failure resistant topology optimization of structures using nonlocal elastoplastic-damage model. Struct Multidiscip Optim, vol 58

Luo Y, Wang MY, Kang Z (2015) Topology optimization of geometrically nonlinear structures based on an additive hyperelasticity technique. Comput Methods Appl Mech Eng 286:422–441

Martí R, Lozano JA, Mendiburu A, Hernando L (2016) Multi-start methods. In: Handbook of heuristics, pp 1–21

Maute K, Schwarz S, Ramm E (1998) Adaptive topology optimization of elastoplastic structures. Struct Optim 15(2):81–91

Miche U (1904) The limits of economy of material in frame structure. Philos Mag 8:589–597

Nakshatrala P, Tortorelli D (2015) Topology optimization for effective energy propagation in rate-independent elastoplastic material systems. Comput Methods Appl Mech Eng 295:305–326

Nakshatrala PB, Tortorelli D, Nakshatrala K (2013) Nonlinear structural design using multiscale topology optimization. Part i: static formulation. Comput Methods Appl Mech Eng 261:167–176

Pedersen CB (2003) Topology optimization design of crushed 2d-frames for desired energy absorption history. Struct Multidiscip Optim 25(5–6):368–382

Pedersen CB (2004) Crashworthiness design of transient frame structures using topology optimization. Comput Methods Appl Mech Eng 193(6–8):653–678

Ramos AS, Paulino GH (2015) Convex topology optimization for hyperelastic trusses based on the ground-structure approach. Struct Multidiscip Optim 51(2):287–304

Rozvany GI, Lewinski T (2014) Topology optimization in structural and continuum mechanics. Springer, New York

Schwarz S, Maute K, Ramm E (2001) Topology and shape optimization for elastoplastic structural response. Comput Methods Appl Mech Eng 190(15–17):2135–2155

Sigmund O (1994) Design of material structures using topology optimization. PhD thesis, Technical University of Denmark, Denmark

Sivaselvan MV, Reinhorn AM (2000) Hysteretic models for deteriorating inelastic structures. J Eng Mech 126(6):633–640

Swan CC, Kosaka I (1997) Voigt-reuss topology optimization for structures with nonlinear material behaviors. Int J Numer Methods Eng 40(20):3785–3814

The MathWorks Inc. (2018) MATLAB- Optimization toolbox, Version 8.1. The MathWorks Inc., Natick

Tortorelli DA (1992) Sensitivity analysis for non-linear constrained elastostatic systems. Int J Numer Methods Eng 33(8):1643–1660

Triantafyllou SP, Koumousis VK (2011) An inelastic timoshenko beam element with axial–shear–flexural interaction. Comput Mech 48(6):713–727

Triantafyllou S, Koumousis V (2012) Small and large displacement dynamic analysis of frame structures based on hysteretic beam elements. J Eng Mech 138(1):36–49

Tsay J, Arora J (1990) Nonlinear structural design sensitivity analysis for path dependent problems. Part 1: general theory. Comput Methods Appl Mech Eng 81(2):183–208

Wallin M, Jönsson V, Wingren E (2016) Topology optimization based on finite strain plasticity. Struct Multidiscip Optim 54(4):783–793

Yuge K, Kikuchi N (1995) Optimization of a frame structure subjected to a plastic deformation. Struct Optim 10(3–4):197–208

Yuge K, Iwai N, Kikuchi N (1999) Optimization of 2-d structures subjected to nonlinear deformations using the homogenization method. Struct Optim 17(4):286–299

Zhang G, Li L, Khandelwal K (2017a) Topology optimization of structures with anisotropic plastic materials using enhanced assumed strain elements. Struct Multidiscip Optim 55(6):1965–1988

Zhang X, Ramos AS, Paulino GH (2017b) Material nonlinear topology optimization using the ground structure method with a discrete filtering scheme. Struct Multidiscip Optim 55(6):2045–2072

Zhang XS, Paulino GH, Ramos AS (2018) Multi-material topology optimization with multiple volume constraints: a general approach applied to ground structures with material nonlinearity. Struct Multidiscip Optim 57(1):161–182